



Cite this: *RSC Adv.*, 2025, 15, 40439

# Comprehensive structural and DFT analysis of a newly synthesized bismuth-based organic–inorganic hybrid material: in-depth insights into vibrational, optical, and photoluminescence properties of $(\text{C}_8\text{H}_{14}\text{N}_2)_2[\text{Bi}_2\text{Br}_{10}] \cdot 2\text{H}_2\text{O}$

Amin Alibi,<sup>a</sup> Nour Elleuch,<sup>a</sup> Sergiu Shova,<sup>b</sup> Jerome Lhoste,<sup>c</sup> Guillaume Duval<sup>c</sup> and Mohamed Boujelbene <sup>\*a</sup>

A newly synthesized bismuth-based organic–inorganic hybrid material,  $(\text{C}_8\text{H}_{14}\text{N}_2)_2[\text{Bi}_2\text{Br}_{10}] \cdot 2\text{H}_2\text{O}$ , was synthesized using a slow evaporation technique and thoroughly characterized to explore its structural, vibrational, optical, and electronic properties. Single-crystal X-ray diffraction confirmed its monoclinic crystal system with a centrosymmetric  $P2_1/c$  space group, featuring edge-sharing  $[\text{Bi}_2\text{Br}_{10}]^{4-}$  dimers interconnected via non-covalent interactions. Hirshfeld surface analysis and fingerprint plots revealed dominant  $\text{H} \cdots \text{Br}$  and  $\text{H} \cdots \text{H}$  interactions, highlighting the role of hydrogen bonding in stabilizing the crystalline architecture. Vibrational studies using FTIR and Raman spectroscopy provided detailed assignments of molecular vibrations, corroborated by density functional theory (DFT) calculations. The optical properties were investigated through UV-vis spectroscopy in solution and diffuse reflectance spectroscopy (DRS) in the solid state, revealing an indirect band gap of 2.9 eV (solid-state) and 3.086 eV (solution), validated by theoretical electronic structure calculations. Photoluminescence (PL) studies demonstrated a strong blue and rose emission, supported by CIE chromaticity analysis, positioning this material as a promising candidate for optoelectronic applications. Additionally, advanced DFT analyses, including electron localization function (ELF), localized orbital locator (LOL), reduced density gradient (RDG), and non-covalent interaction (NCI) analyses, provided deep insights into electronic charge distribution, weak intermolecular interactions, and structural stability. These findings establish  $(\text{C}_8\text{H}_{14}\text{N}_2)_2[\text{Bi}_2\text{Br}_{10}] \cdot 2\text{H}_2\text{O}$  as a bismuth-based hybrid material with significant potential in optoelectronics, luminescent materials, and functional optical applications.

Received 3rd September 2025  
Accepted 24th September 2025

DOI: 10.1039/d5ra06614j

rsc.li/rsc-advances

## 1. Introduction

The deliberate synthesis and design of organic–inorganic hybrid materials incorporating divalent or trivalent post-transition metal halides, particularly Bismuth-based compounds, have attracted significant scientific interest. This is due to their unique structural features, distinctive chemical and physical properties, and multifunctionality, making them promising for applications in optoelectronics, data communication, switchable dielectric devices, and rewritable optical data storage.<sup>1–3</sup> A key aspect of  $\text{Bi(III)}$  is its ability to form polynuclear anionic halide complexes, and its lower toxicity compared to

lead has driven efforts toward environmentally friendly alternatives.  $\text{Bi(III)}$  exhibits diverse structural types, including discrete anions with varying nuclearity, one-dimensional coordination polymers,<sup>4–6</sup> and heterometallic derivatives.

Beyond structural interest, these compounds exhibit ferroelasticity, semiconductivity,<sup>7–10</sup> thermochromism,<sup>11–13</sup> and photochromism,<sup>14–16</sup> though optimizing multiple properties within a single material remains challenging. The impact of structural phase transitions on electrical properties is still not fully understood, limiting material design predictability. While luminescence studies on polynuclear  $\text{Bi(III)}$  halides (polyhalide bismuthates, PHBs) have increased,<sup>17–19</sup> they remain relatively sparse. Luminescence typically originates from aromatic cations, while PHB crystal packing significantly influences optical properties.<sup>20</sup> These hybrid materials, represented by the general formula  $\text{RaMbX}(3b+a)$  ( $\text{X} = \text{Cl}, \text{Br}, \text{I}$ ;  $\text{M} = \text{Sb(III)}, \text{Bi(III)}$ ;  $\text{R} = \text{organic cation}$ ), form discrete or polyoctahedral anions in 0D to 3D networks.<sup>21,22</sup>

<sup>a</sup>Laboratory of Physico-Chemistry of Solid State, LR11ES51, Sfax Faculty of Sciences, University of Sfax, Sfax 3000, Tunisia

<sup>b</sup>“Petru Poni” Institute of Macromolecular Chemistry, Alea Grigore Ghica Voda 41-A, 700487 Iasi, Romania

<sup>c</sup>MMM-UMR 6283 CNRS, Lunam, Faculty of Sciences and Techniques, University of Maine, Avenue Olivier Messiaen, 72085, Le Mans Cedex 9, France


This article is divided into two main sections. The first examines the crystal structure and molecular composition of  $(\text{C}_8\text{H}_{14}\text{N}_2)_2[\text{Bi}_2\text{Br}_{10}]\cdot 2\text{H}_2\text{O}$  using SCXRD, FT-IR, Raman spectroscopy, and Hirshfeld surface analysis to understand molecular geometry, vibrational modes, and intermolecular interactions, with a focus on hydrogen bonding and halogen coordination. The second section explores its optical and luminescence properties, emphasizing material applications, supported by in-depth DFT calculations. The interplay between the organic cation and the Bi-Br framework is analyzed to understand tunable physical properties such as solvatochromism and photoluminescence. This study aims to expand knowledge of bismuth halides for advanced material development.

We present the synthesis, DFT calculations, and in-depth analysis of bis(*N,N'*-di(4-ethyl aminomethyl)pyridinium) decabromodibismuthate(III) dihydrate, focusing on its structural, vibrational, and optical properties. Key techniques include XRD, Hirshfeld surface analysis, IR and Raman spectroscopy, and optical studies through photoluminescence (PL) and UV-vis spectroscopy in both liquid and solid states. DFT calculations (Gaussian 09W and Multiwfn) provide insights into its electronic structure. This research contributes to the growing understanding of bismuth-based hybrids, addressing structure–performance relationships to facilitate high-efficiency, stable material design.

## 2. Experimental

### 2.1. Materials and characterization techniques

A new hybrid material was synthesized by combining commercially available reagents,  $\text{BiBr}_3$  and  $\text{HBr}$ , with the organic compound  $\text{C}_8\text{H}_{12}\text{N}_2$ , without further purification of the chemicals. The functional groups and molecular structure of the synthesized compound were identified using infrared spectroscopy. FT-IR spectra were recorded at room temperature with a PerkinElmer FTIR Spectrometer, covering the range of  $4000\text{--}500\text{ cm}^{-1}$ . In addition, Raman spectroscopy was performed to analyze the compound's vibrational modes, using a Horiba/Jobin Yvon T6400 spectrometer within the range of  $4000\text{--}50\text{ cm}^{-1}$ .

The optical properties of the synthesized material were investigated by recording the diffuse reflectance spectra (DRS) at room temperature using a PerkinElmer Lambda 35 UV-vis spectrophotometer equipped with an integrating sphere. An 8 mm diameter sample pellet was used, and spectra were captured in the range of 200 to 1100 nm. Furthermore, UV-vis spectra in aqueous solution were obtained using a Cary 5000 UV-vis-NIR spectrophotometer, within the 250–600 nm range. The photoluminescence properties of the compound were assessed at room temperature using a PerkinElmer LS 55 spectrometer. The sample was dissolved in a suitable solvent to prepare a clear solution, which was placed in a quartz cuvette for measurement. The emission spectrum was recorded under ambient conditions using excitation wavelengths of 319 and 350 nm. The relationship between the UV-vis spectra in both liquid and solid states, along with the TD-DFT analysis, was

employed to further confirm the energy gap and to ascertain whether the band gap corresponds to a direct or indirect transition.

### 2.2. Synthesis of $(\text{C}_8\text{H}_{14}\text{N}_2)_2[\text{Bi}_2\text{Br}_{10}]\cdot 2\text{H}_2\text{O}$

The new hybrid material with the chemical formula  $(\text{C}_8\text{H}_{14}\text{N}_2)_2[\text{Bi}_2\text{Br}_{10}]\cdot 2\text{H}_2\text{O}$  was successfully synthesized using the slow evaporation method at ambient temperature (approximately  $30^\circ\text{C}$ ). The preparation involved separately dissolving 4-ethyl aminomethyl pyridine ( $\text{C}_8\text{H}_{12}\text{N}_2$ ) and  $\text{BiBr}_3$  (98% purity) in distilled water, maintaining a 1 : 1 molar ratio. Each solution was stirred for about 30 minutes to achieve uniform mixing. After combining the solutions, concentrated hydrobromic acid ( $\text{HBr}$ , 48% purity) was carefully introduced in three equal portions at intervals of 30 minutes, with the mixture continuously stirred. Following the final addition, the solution was stirred for another 30 minutes, resulting in a total stirring duration of 1.5 hours.

The combined solution was left undisturbed for four days to allow crystal formation through slow evaporation. This process produced yellow plate-shaped crystals with consistent morphology. The crystals were collected through filtration, and a single crystal was selected for detailed structural analysis using single-crystal X-ray diffraction. The synthesis method was straightforward and reproducible, with no difficulties encountered. Furthermore, the compound exhibited good stability under normal storage conditions without requiring special precautions.

The compositional purity and structural integrity of the compound  $(\text{C}_8\text{H}_{14}\text{N}_2)_2[\text{Bi}_2\text{Br}_{10}]\cdot 2\text{H}_2\text{O}$  were first assessed by energy-dispersive X-ray spectroscopy (EDS) combined with elemental mapping, as presented in the upper part of Fig. 1.S. The EDS spectrum displays exclusively the characteristic peaks of nitrogen, bromine, and bismuth, with no detectable contributions from extraneous elements, thereby confirming the excellent chemical purity of the synthesized material. The corresponding elemental distribution maps further demonstrate the homogeneous dispersion of Br and Bi across the crystalline domains, while the nitrogen signal highlights the uniform incorporation of the organic cations within the hybrid lattice. It is worth noting that carbon, oxygen, and hydrogen atoms are not observed in the EDS results. This limitation is inherent to the technique: hydrogen cannot be detected at all due to its extremely low atomic number, while carbon and oxygen, although present in the organic cations and hydration water, often produce weak or unreliable signals that are absorbed or overlap with background noise. For this reason, EDS predominantly provides information on the heavier inorganic elements, and its results are interpreted accordingly. Importantly, the absence of any additional signals beyond N, Br, and Bi unambiguously confirms the high purity and compositional integrity of the compound.

Complementary structural characterization was performed using powder X-ray diffraction (PXRD), shown in the lower part of Fig. 1.S. The experimental diffractogram (red curve) reveals sharp and well-defined reflections, indicative of a high degree of



crystallinity, and matches closely with the simulated pattern calculated from the single-crystal structural data (black curve). The excellent agreement in both peak positions and intensities excludes the presence of secondary phases and validates the proposed structural model of the dimeric bismuth–bromide hybrid material  $(\text{C}_8\text{H}_{14}\text{N}_2)_2[\text{Bi}_2\text{Br}_{10}]\cdot 2\text{H}_2\text{O}$ . Together, the EDS and PXRD analyses unequivocally confirm both the compositional and structural purity of the material.

### 2.3. Single-crystal X-ray data collection and structure determination

The crystal structure of  $(\text{C}_8\text{H}_{14}\text{N}_2)_2[\text{Bi}_2\text{Br}_{10}]\cdot 2\text{H}_2\text{O}$  was determined using single-crystal X-ray diffraction (SCXRD) at 293 K. Data processing and analysis were carried out using the Olex2-1.5 software package,<sup>23</sup> with structure solution performed by direct methods (SHELXT 2018/2 ref. 24) and refinement using full-matrix least squares on  $F^2$  (SHELXL 2018/3 ref. 25). The experiment was conducted with Mo-K $\alpha$  radiation ( $\lambda = 0.71073$  Å) on an XtaLAB Synergy, Dualflex, HyPix diffractometer, using a selected crystal of dimensions  $0.1 \times 0.1 \times 0.03$  mm<sup>3</sup>. Anisotropic displacement parameters were applied to all non-hydrogen atoms, while hydrogen atoms were positioned using the HFIX command with the following constraints: CH<sub>2</sub> and NH<sub>2</sub> were assigned the value 23, CH<sub>3</sub> was assigned 137, NH and CH of the aromatic cycle were assigned 43, and H<sub>2</sub>O was assigned 6. The final refinement cycle yielded excellent agreement factors, with  $R_1 = 2.31\%$  and  $wR_2 = 5.53\%$ , indicating

high structural accuracy. To visualize the molecular arrangement, intermolecular forces, and symmetry elements within the crystal lattice, DIAMOND 3 software<sup>26</sup> was used to generate structural figures and packing interaction diagrams. The full crystallographic refinement parameters are summarized in Table 1.

### 2.4. Hirshfeld surface analysis

Hirshfeld surface analysis<sup>27–34</sup> partitions the electron density of a crystal into molecular fragments, enabling visualization and quantification of non-covalent interactions such as hydrogen bonding,  $\pi$ – $\pi$  stacking, and halogen bonding.<sup>35,36</sup> This technique provides critical insights into molecular packing and intermolecular forces.

To highlight these interactions, 2D fingerprint plots<sup>37,38</sup> were generated using Crystal Explorer 21.5 software,<sup>39</sup> with the CIF file as input. These plots map the frequency and type of intermolecular contacts. Each point on the Hirshfeld isosurface is defined by two key distances:

$d_i$ : distance from the surface to the nearest nucleus inside the molecule.  $d_e$ : distance from the surface to the nearest nucleus in neighboring molecules.

The normalized contact distance ( $d_{\text{norm}}$ ) is computed as:

$$d_{\text{norm}} = \frac{d_i - r_{\text{vdw}}}{r_{\text{vdw}}} + \frac{d_e - r_{\text{vdw}}}{r_{\text{vdw}}}$$

where  $r_{\text{vdw}}$  and  $r_{\text{evdw}}$  are the van der Waals radii of interacting atoms.<sup>40,41</sup>

This analysis identifies interaction regions, with red, white, and blue representing short, moderate, and long contacts, respectively. The 2D fingerprint plots quantify the percentage contributions of different non-covalent interactions, offering a detailed understanding of the crystal packing forces in our hybrid material.

### 2.5. Computational details

The computational investigation of the hybrid material  $(\text{C}_8\text{H}_{14}\text{N}_2)_2[\text{Bi}_2\text{Br}_{10}]\cdot 2\text{H}_2\text{O}$  was conducted to examine its structural, electronic, and optical properties. All calculations were performed using density functional theory (DFT) with the B3LYP functional<sup>42</sup> and the LanL2DZ basis set<sup>43</sup> in the Gaussian 09W package.<sup>44</sup> A cluster model consisting of two water molecules, two organic cations  $(\text{C}_8\text{H}_{14}\text{N}_2)^{2+}$ , and a  $[\text{Bi}_2\text{Br}_{10}]^{4-}$  dimer was optimized, allowing full relaxation of parameters to ensure energy minimization. Vibrational frequencies were calculated to assign vibrational modes, which were compared with experimental data, with assignments primarily derived from DFT and visually analyzed using GaussView 6.0.16.<sup>45</sup> Additionally, partial density of states (PDOS), electron localization function (ELF), localized orbital locator (LOL), and electrostatic potential (ESP) were obtained *via* Multiwfn software.<sup>46</sup> The UV-vis absorption spectra were also calculated and compared with experimental results to gain deeper insight into the material's optical behavior.

The decision to omit the GENIECP option was based on two factors. First, its computational cost is significantly higher than

Table 1 Summary of crystal data and structure refinement details

Crystallographic data	
Empirical formula	$(\text{C}_8\text{H}_{14}\text{N}_2)_2[\text{Bi}_2\text{Br}_{10}]\cdot 2\text{H}_2\text{O}$
Color/shape	Yellow/plate
Molar mass (g mol <sup>−1</sup> )	1529.51
Diffractometer	XtaLAB synergy, Dualflex, HyPix diffractometer
Radiation type	Mo K $\alpha$ (0.71073 Å)
Temperature (K)	293
Calculated density (Mg m <sup>−3</sup> )	2.950
Crystal system	Monoclinic
Space group	$P2_1/c$
$Z/Z'$	2/0.5
Unit cell parameters $a$ (Å)	10.6409 (2)
$b$ (Å)	12.0862 (2)
$c$ (Å)	14.1356 (4)
$\beta$ (°)	108.685 (3)
Absorption coefficient (mm <sup>−1</sup> )	21.83
Number of reflections	$h = -12 \rightarrow 12$ ,
measured variation of $h, k, l$	$k = -13 \rightarrow 14, l = -16 \rightarrow 16$
Scanning range of $\theta$ (°)	$2.6 < \theta < 30.2$
$F(000)$	1376
Independent parameters	159
$\Delta\rho_{\text{max}}/\Delta\rho_{\text{min}}$ (e Å <sup>−3</sup> )	1.89/−1.05
$(\Delta/\sigma)_{\text{max}}$	< 0.001
$R[F^2 > 2\sigma(F^2)] = R_1$	0.023
$wR(F^2) = wR_2$	0.055
$S = \text{Goof}$	1.07
CCDC	2384365



LANL2DZ, making it less efficient. Second, while GENECP is often preferred for heavy metals due to its accuracy, the LANL2DZ results showed minimal deviation, providing sufficiently precise data. Given this close agreement, the more computationally demanding GENECP was deemed unnecessary.

### 3. Results and discussion

#### 3.1. Crystal structure

A comprehensive understanding of a new hybrid material's properties and potential applications requires a detailed structural description. In this study, we synthesized a bromobismuthate(III)-based organic-inorganic hybrid material,  $(C_8H_{14}N_2)_2[Bi_2Br_{10}] \cdot 2H_2O$ , which crystallizes in the monoclinic crystal system (first setting). This material belongs to the centrosymmetric space group  $P2_1/c$ , characterized by four symmetry operations: identity, inversion, a 2-fold screw axis along the  $b$ -axis, and an axial glide plane ( $c$ ) perpendicular to the  $b$ -axis. The structure features a primitive monoclinic unit cell with inversion symmetry centered on the  $[Bi_2Br_{10}]^{4-}$  dimer, resulting in an asymmetric unit comprising half of the formula unit ( $Z' = 0.5$ ). The unit cell contains two formula units ( $Z = 2$ ), as determined by the symmetry elements and the  $Z'$  value. The refined lattice parameters for this compound are  $a = 10.6409(2) \text{ \AA}$ ,  $b = 12.0862(2) \text{ \AA}$ ,  $c = 14.1356(4) \text{ \AA}$ , and  $\beta = 108.685(3)^\circ$ .

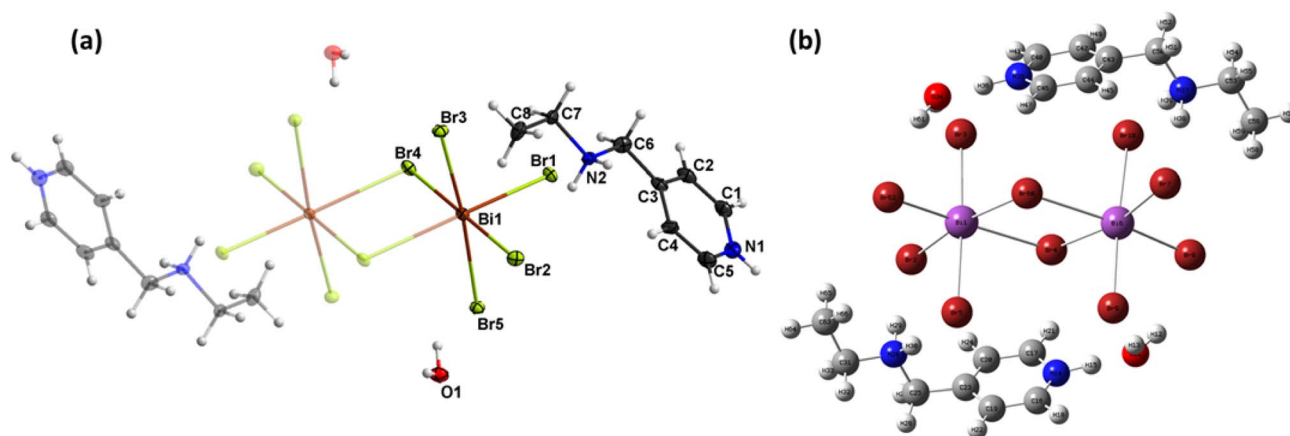
Fig. 1(a), generated using DIAMOND 3, presents both the asymmetric unit and the full formula unit, which consists of two diprotonated organic cations  $(C_8H_{14}N_2)^{2+}$ , one  $[Bi_2Br_{10}]^{4-}$  dimer, and two  $H_2O$  molecules. The structure exhibits no atomic disorder or structural defects, ensuring high structural stability, as confirmed by the normal ellipsoid volumes in Fig. 1(a). Additionally, no excess electron density or unresolved disorder was detected. A summary of the lattice parameters, unit cell volume, and crystallographic details is provided in Table 1, while Table 1.S lists the atomic positions and their thermal agitation factors ( $U_{eq}$ ).

Fig. 1(b) illustrates the optimized geometry of the formula unit, highlighting the calculated bond distances. A comparison between theoretical and experimental bond lengths shows that most optimized bond lengths are slightly longer than their experimental counterparts. This discrepancy is expected, as theoretical calculations consider an isolated molecule, whereas experimental measurements reflect a solid-state environment influenced by intermolecular interactions and crystal packing effects. These findings validate the accuracy of our computational approach, confirming that the B3LYP/LanL2DZ level of theory is well-suited for this system.

Fig. 2 offers valuable insights into the crystalline structure. The projection along the  $b$ -axis reveals that the inorganic entities are arranged in parallel associations along the  $c$ -axis. The anionic components occupy two distinct positions within the unit cell along the  $c$ -axis: one at the corners and the other at the center of the faces parallel to the  $c$ -axis. Notably, these anionic components are stabilized by water molecules surrounding the polyhedra and the positive charge from the protonated nitrogen atoms of the organic cations.

Fig. 2.S illustrates notable variations in Bi-Br bond lengths, which range from  $2.7271(5) \text{ \AA}$  to  $3.0612(5) \text{ \AA}$ . The Br-Bi-Br bond angles exhibit a broad distribution, spanning  $87.274(13)^\circ$  to  $94.257(15)^\circ$  for cis configurations and  $174.713(14)^\circ$  to  $177.625(14)^\circ$  for trans configurations. The most significant bond length difference of  $0.3341 \text{ \AA}$  is observed between two opposing halogen atoms (Bi-Br1 and Bi1-Br4i). A comprehensive summary of the geometric parameters, including bond angles and distances for the anionic groups, is provided in Table 2.S.

Furthermore, the presence of hydrogen bonding involving the bromine atoms influences the lone electron pair of the Bi atom, causing a shift in electron density toward the hydrogen atom. This shift reduces the electron density around the bridging Br atom, leading to an elongation of the Bi-Br bonds. As a result, the bond length variations and angular deviations contribute to a slight distortion of the  $BiBr_6$  octahedral geometry, quantified by an octahedral distortion index of  $ID(Bi-Br) = 1.7 \times 10^{-6}$ . This distortion originates from a combination of





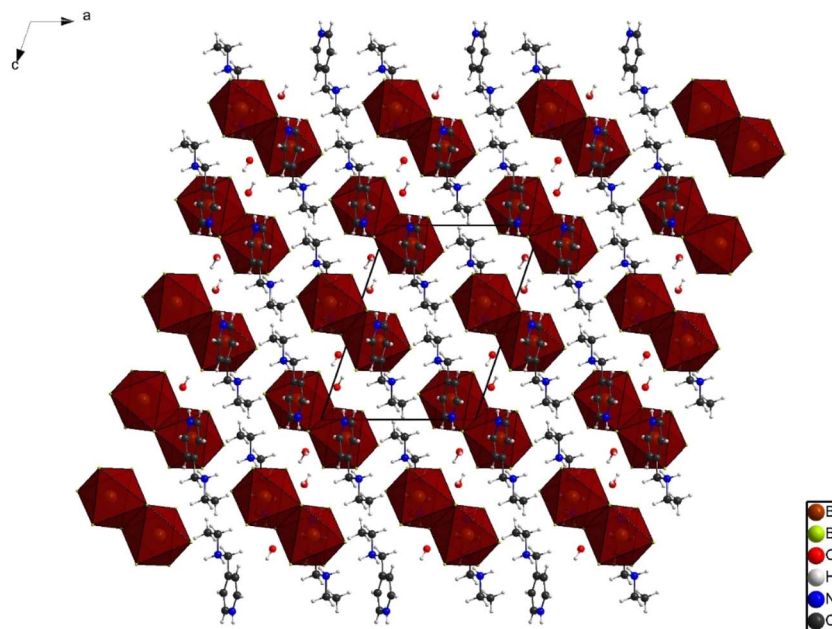


Fig. 2 Projection of the unit cell of  $(\text{C}_8\text{H}_{14}\text{N}_2)_2[\text{Bi}_2\text{Br}_{10}]\cdot 2\text{H}_2\text{O}$  structure along the crystallographic  $b$ -axis.

primary deformations, driven by the stereochemical activity of Bi's lone electron pair, and secondary deformations, induced by hydrogen bonding interactions.

$$\text{ID}(\text{Bi} - \text{Br}) = \frac{1}{6} \sum_i \left| \frac{\text{BiBr}_i - \text{BiBrm}}{\text{BiBrm}} \right| = 1.7 \times 10^{-6}$$

The spatial arrangement of atoms or ions within a crystal lattice plays a crucial role in determining a material's physical properties, including mechanical strength and thermal conductivity. Assessing the efficiency of this arrangement can be achieved through both direct and indirect methods. One of the most straightforward measures is crystal density, where a higher density signifies more efficient atomic or ionic packing. In this study, our hybrid material exhibits a remarkably high density of  $2.950 \text{ g cm}^{-3}$ , indicating a highly efficient packing arrangement.

An alternative approach to evaluating packing efficiency is void analysis, which quantifies the presence of unoccupied spaces or pores within the crystal structure. The extent of these voids directly impacts the material's packing efficiency and influences its macroscopic properties. As part of our Hirshfeld surface analysis, we conducted a crystal void analysis to gain further insight into the packing efficiency. The results of this analysis were in strong agreement with the density measurement, reinforcing the conclusion that the crystal structure of our material is highly efficient.

Conjugation refers to the extended delocalization of  $\pi$ -electrons across alternating single and multiple bonds through overlapping p-orbitals. The studied organic molecule possesses three conjugated forms, leading to extensive electron delocalization that significantly influences its electronic, optical, and chemical properties. Fig. 3.S illustrates the spatial arrangement

of the organic molecules within the unit cell, where two di-protonated organic cations align parallel to the  $(b,c)$  plane. Key geometric parameters, including bond angles and interatomic distances of the organic groups, are summarized in Table 3.S, providing a detailed structural analysis.

The crystal's structural integrity is governed by an intricate arrangement of molecules interconnected *via* hydrogen bonding. Within this framework, three distinct bond types are observed:  $\text{O}-\text{H}\cdots\text{Br}$ ,  $\text{N}-\text{H}\cdots\text{O}$ , and  $\text{N}-\text{H}\cdots\text{Br}$ , totaling four hydrogen bonds. The cohesive forces and physical characteristics of the crystal hinge upon these bonding interactions. Specifically, the water molecules engage with both organic cations and nitrogen atoms, fostering cohesion between them and facilitating the formation of a three-dimensional lattice. The strength of hydrogen bonds associated with halogen atoms can be delineated into weak and strong categories based on the Brown criteria,<sup>47</sup> where bonds with  $d_{\text{D}-\text{A}}$  distances exceeding  $3.19 \text{ \AA}$  are considered weak, and those below are deemed strong. Applying this criterion, bonds such as  $\text{O}_1-\text{H}_{1\text{C}}\cdots\text{Br}_5^{\text{ii}}$ ,  $\text{N}_2-\text{H}_{2\text{B}}\cdots\text{Br}_5^{\text{iii}}$ , and  $\text{N}_2-\text{H}_{2\text{A}}\cdots\text{Br}_2$  are classified as weak. For the determination of  $\text{N}-\text{H}\cdots\text{O}$  hydrogen bond strength, the R. H. Blessing criteria<sup>48</sup> prescribe a threshold distance of  $d_{\text{D}-\text{A}} = 2.7 \text{ \AA}$ , categorizing the  $\text{N}_1-\text{H}_1\cdots\text{O}_1^{\text{iv}}$  bond as strong. Fig. 3 illustrates these hydrogen bonds within the asymmetric unit and unit cell, with their replication evident through inversion symmetry at the center. A detailed account of the distances and angles of these bonds is presented in Table 2.

### 3.2. Vibrational studies

Fourier Transform Infrared (FTIR) spectroscopy and Raman scattering analyses were performed at room temperature to investigate the functional groups and gain structural insights into the crystal. The FTIR study primarily focused on the



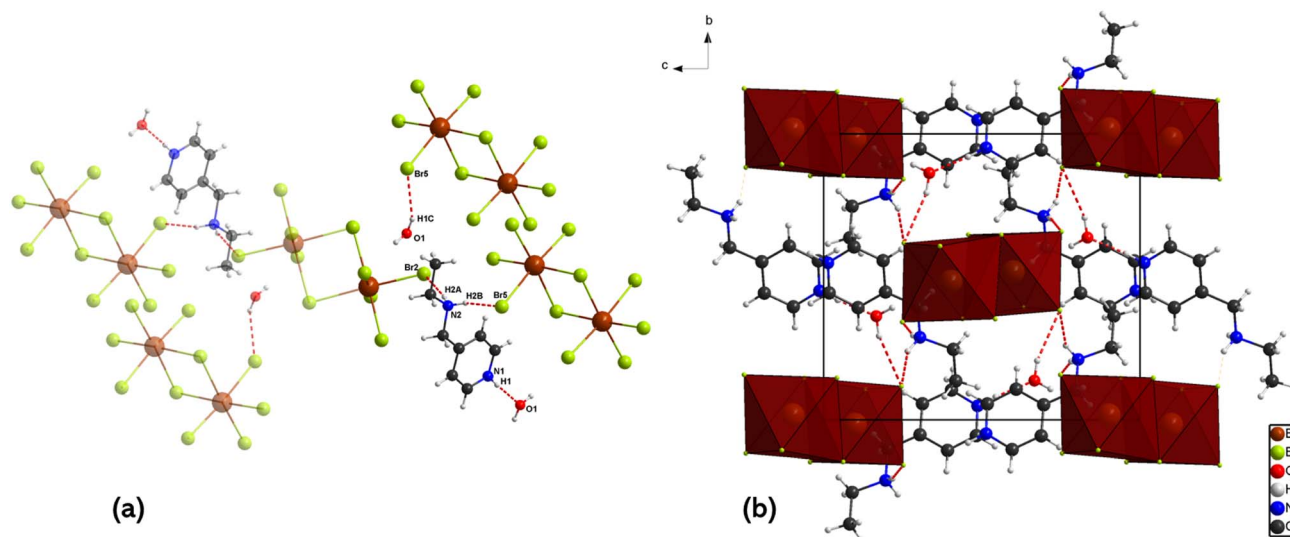


Fig. 3 The arrangement of hydrogen bonds between water molecules, organic cations, and inorganic  $[\text{Bi}_2\text{Br}_{10}]^{4-}$  ions: (a) in the formula unit and (b) in the unit cell.

Table 2 Interatomic distances and hydrogen bond angles of the compound<sup>a</sup>

D–H...A	D–H (Å)	H...A (Å)	D...A (Å)	D–H...A (°)
O1–H1C...Br5 <sup>ii</sup>	0.85	2.61	3.389 (4)	153
N1–H1...O1 <sup>iii</sup>	0.86	1.83	2.684 (6)	170
N2–H2A...Br2	0.89	2.62	3.494 (4)	169
N2–H2B...Br5 <sup>iv</sup>	0.89	2.53	3.301 (4)	146

<sup>a</sup> Symmetry codes: (ii)  $-x, y - 1/2, -z + 3/2$ ; (iii):  $-x + 1, -y + 1, -z + 2$ ; (iv):  $-x + 1, y - 1/2, -z + 3/2$ .

vibrational modes of the organic cation, as the heavier inorganic anion vibrations remained undetectable due to their large mass. Conversely, Raman spectroscopy was employed to characterize the vibrational features of the anionic framework. To ensure accurate spectral band assignments, Density Functional Theory (DFT) calculations were carried out.

A comparative analysis of experimental and theoretical FTIR spectra is illustrated in Fig. 4, while Fig. 5 presents the experimental and theoretical Raman spectra of  $(\text{C}_8\text{H}_{14}\text{N}_2)_2[\text{Bi}_2\text{Br}_{10}] \cdot 2\text{H}_2\text{O}$ . The vibrational mode assignments, along with their corresponding experimental and calculated wavenumbers, are summarized in Table 4.S, demonstrating a strong correlation between theoretical predictions and observed spectral data. The close agreement between experimental and computed frequencies supports the reliability of the proposed spectral assignments. While periodic calculations could provide an even more precise description of the system, their application is often restricted due to substantial computational demands.

**3.2.1  $[\text{Bi}_2\text{Br}_{10}]^{4-}$  vibrational modes.** The Raman spectrum of  $(\text{C}_8\text{H}_{14}\text{N}_2)_2[\text{Bi}_2\text{Br}_{10}] \cdot 2\text{H}_2\text{O}$  exhibits a prominent absorption band at shorter wavelengths, indicative of the presence of the bismuth complex  $[\text{Bi}_2\text{Br}_{10}]^{4-}$ , which adopts the dimer octahedral geometry. Experimental analysis has identified several

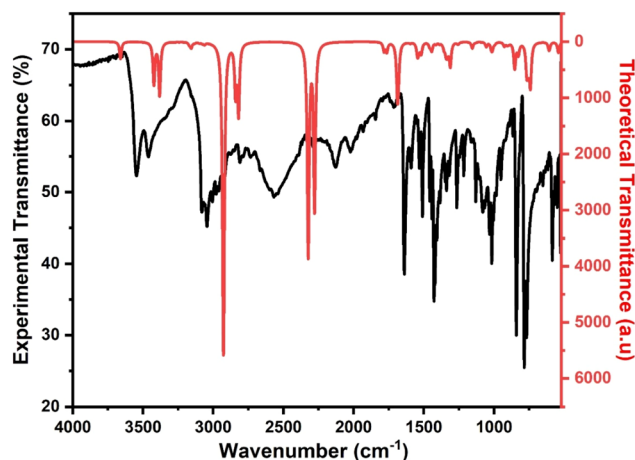


Fig. 4 FT-IR spectrum of the title compound.

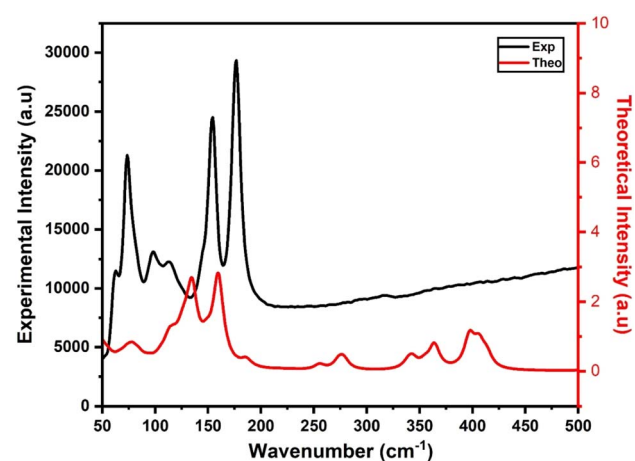


Fig. 5 Raman spectrum of the title compound.



vibrational modes within the 50 to 200  $\text{cm}^{-1}$  range, corroborated by theoretical predictions. Notably, this spectral region displays two peaks for deformation vibrational modes and two peaks for symmetric and asymmetric stretching vibrational modes, respectively at 98, 154, 113, and 176  $\text{cm}^{-1}$ . Theoretical calculations suggest that the expected frequencies for these vibrational modes of  $[\text{Bi}_2\text{Br}_{10}]^{4-}$  are 112, 160, 133, and 185  $\text{cm}^{-1}$ , respectively.

**3.2.2  $(\text{C}_8\text{H}_{14}\text{N}_2)^{2+}$  vibrational modes.** The table of vibrational frequencies provides an analysis of the IR and Raman spectra, comparing experimental and theoretical vibrational modes for key bonds in the compound. For water molecules ( $\text{H}_2\text{O}$ ), the asymmetric stretching mode appears at 3578  $\text{cm}^{-1}$  in the IR spectrum, with a calculated frequency of 3660  $\text{cm}^{-1}$ , while the symmetric stretching mode is observed at 3451  $\text{cm}^{-1}$ , with a theoretical counterpart at 3423  $\text{cm}^{-1}$ . These vibrational modes indicate strong interactions involving water molecules, essential for stabilizing the hybrid structure. The  $\text{NH}_2$  group also exhibits characteristic vibrations, including asymmetric stretching at 3035  $\text{cm}^{-1}$  (calculated at 2930  $\text{cm}^{-1}$ ) and symmetric stretching at 2814  $\text{cm}^{-1}$  (theoretically assigned to 2841  $\text{cm}^{-1}$ ), reflecting the vibrational behavior of the organic cation.

The table further highlights vibrational modes for ethyl groups, such as  $\text{CH}_2$  asymmetric stretching at 3160  $\text{cm}^{-1}$  and  $\text{CH}_3$  at 3081  $\text{cm}^{-1}$ , with theoretical values at 3169 and 3069  $\text{cm}^{-1}$ , respectively. Hydrogen bonding interactions, such as the  $\text{N-H}\cdots\text{O}$  stretching mode, appear in the IR spectrum between 1845–2694  $\text{cm}^{-1}$ , with a theoretical range of 2280–2323  $\text{cm}^{-1}$ , crucial for linking organic cations and water molecules to the inorganic framework.

In the lower wavenumber region, bending and twisting modes are observed, including  $\text{NH}_2$  bending at 1720  $\text{cm}^{-1}$ , water bending at 1651  $\text{cm}^{-1}$ , and  $\text{CH}_2$  deformation at 1508  $\text{cm}^{-1}$ . These modes provide insight into molecular flexibility and dynamics within the hybrid structure. The presence of multiple vibrational modes across frequency regions underscores the material's complex bonding interactions, aligning with computational predictions and validating its structural properties.

### 3.3. Optical study

**3.3.1 UV-vis spectroscopy and photoluminescence properties.** To comprehensively elucidate the optical properties of  $(\text{C}_8\text{H}_{14}\text{N}_2)_2[\text{Bi}_2\text{Br}_{10}]\cdot 2\text{H}_2\text{O}$ , a systematic investigation was conducted using UV-vis spectroscopy in both liquid and solid states, as well as photoluminescence (PL) spectroscopy. This multi-technique approach ensures a thorough understanding of the compound's absorption characteristics, band structure, and charge carrier dynamics. The liquid-state UV-vis absorption spectrum is particularly valuable for probing solute-solvent interactions and the electronic transitions of the complex in a dynamic environment, while the solid-state diffuse reflectance spectroscopy (DRS) provides a more accurate estimation of the optical bandgap, as it directly correlates with the material's bulk properties in its condensed phase. The PL spectrum further

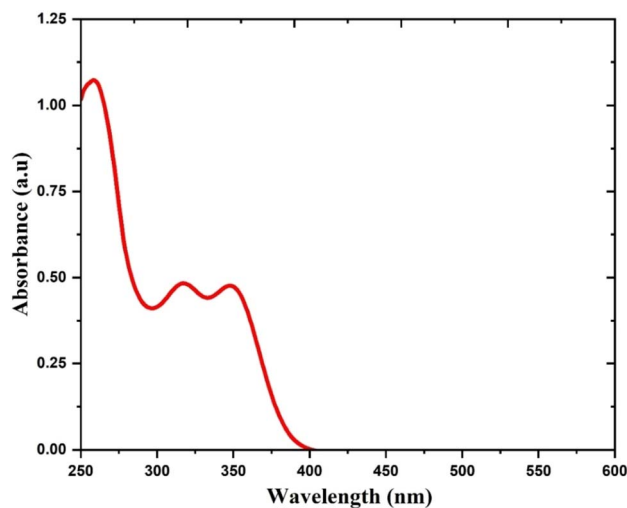


Fig. 6 UV-visible optical absorption.

complements these findings by revealing excitonic behavior and confirming the nature of the electronic transitions. In the UV-vis absorption spectrum (Fig. 6, liquid state), three prominent absorption peaks are identified at 258 nm, 317 nm, and 348 nm, each corresponding to distinct electronic transitions within the hybrid material.

The high-energy absorption at 258 nm is attributed to localized  $\pi \rightarrow \pi$  transitions within the organic moiety, specifically within the aromatic rings of the diprotonated  $(\text{C}_8\text{H}_{14}\text{N}_2)^{2+}$  cations. The absorption feature at 317 nm corresponds to charge transfer transitions within the  $[\text{Bi}_2\text{Br}_{10}]^{4-}$  (LMCT, from Br 4p to Bi 6p), while the most critical absorption peak at 348 nm originates from intramolecular charge transfer transitions within the  $[\text{Bi}_2\text{Br}_{10}]^{4-}$  inorganic sublattices and the organic cation, specifically, Bi 6p + Br 4p  $\rightarrow$  N 2p + C 2p electronic excitations, a characteristic feature of bismuth-based halide hybrids that is also reflected in the density of states (DOS and PDOS) calculations (Fig. 17), where the conduction band minimum (CBM) is dominated by N 2p + C 2p states and the valence band maximum (VBM) consists primarily of Bi 6p + Br 4p orbitals.

Fig. 7 presents the Tauc plots used to determine the optical bandgap of  $(\text{C}_8\text{H}_{14}\text{N}_2)_2[\text{Bi}_2\text{Br}_{10}]\cdot 2\text{H}_2\text{O}$ , distinguishing between direct and indirect electronic transitions. The Tauc method<sup>49</sup> estimates bandgap energies by plotting  $(\alpha h\nu)^n$  versus photon energy ( $h\nu$ ), where  $\alpha$  is the absorption coefficient and  $n$  depends on the transition type:  $n = 2$  for an indirect bandgap (phonon-assisted transitions) and  $n = 1/2$  for a direct bandgap (phonon-independent). For this hybrid material, the  $(\alpha h\nu)^{1/2}$  plot confirms an indirect bandgap, as the direct transition model fails to fit the absorption data. The extracted bandgap values are 3.086 eV in solution (UV-vis, Fig. 6) and 2.9 eV in the solid state (DRS, Fig. 10), in excellent agreement with theoretical calculations using the zero-DOS method (Fig. 17(a)), which predicts 2.85 eV. The zero-DOS approach identifies the band edges by determining the precise energy values at which the DOS first becomes strictly zero, accounting for numerical precision. The



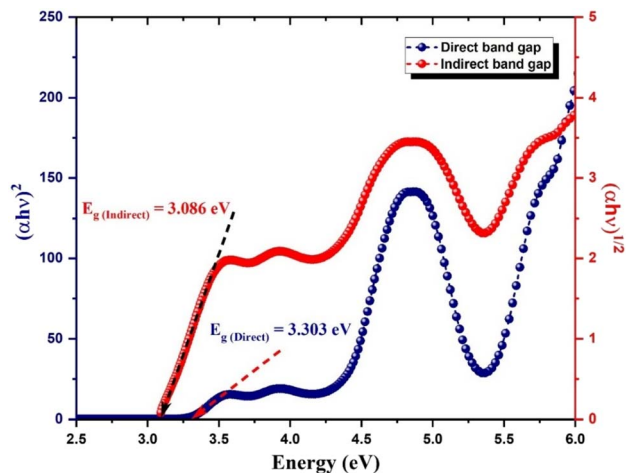


Fig. 7 Direct vs. indirect transitions Tauc plots.

band gap is thus defined as the interval between the last occupied state and the first unoccupied state where the DOS vanishes completely. In contrast, the conventional DOS method typically estimates the band gap from a broadened DOS spectrum, where small non-zero values may appear within the nominal gap due to smearing functions, limited  $k$ -point sampling, or numerical noise.

Fig. 8 presents the photoluminescence (PL) spectrum of  $(C_8H_{14}N_2)_2[Bi_2Br_{10}] \cdot 2H_2O$ , offering detailed insights into the material's excited-state electronic behavior, band structure, and charge carrier dynamics. PL spectroscopy, as applied here, complements the UV-vis absorption (Fig. 6), diffuse reflectance (Fig. 10), and Tauc analysis, serving as a powerful probe for exciton recombination and defect-related emissions. The PL spectrum displays two distinct emission features: a broad band centered around 350 nm and a sharp emission at 706 nm, with an intermediate shoulder near 645 nm. The broad peak at 350 nm is attributed to radiative relaxation of high-energy

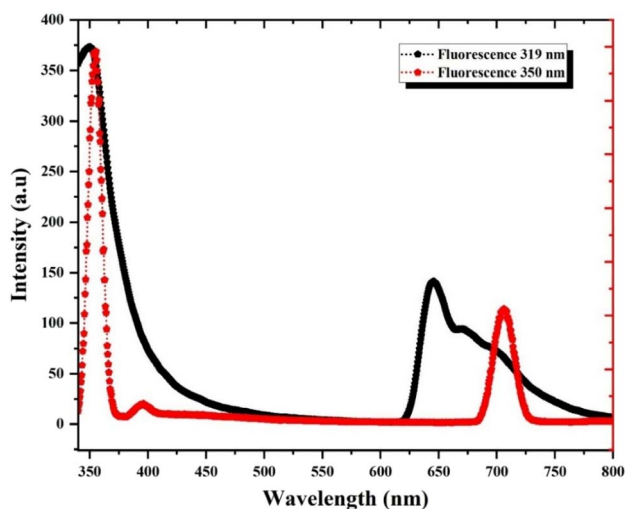


Fig. 8 Emission plot of photoluminescence.

excitons within the  $[Bi_2Br_{10}]^{4-}$  framework, in line with the charge transfer absorption band at 348 nm. The broadening of this emission, alongside its spectral width, indicates phonon-assisted recombination and multiple non-radiative decay pathways, hallmarks of an indirect bandgap system.

The transition from a broad to a sharp emission as the energy decreases reflects a shift from delocalized to more localized recombination processes. The sharp peak at 706 nm, redshifted from the 645 nm shoulder, confirms a significant Stokes shift, supporting an indirect transition where carriers undergo phonon-mediated energy loss prior to recombination. This sharp emission also points to a highly specific and radiatively efficient decay channel with limited energetic disorder, which aligns with the low Urbach energy observed in Fig. 12(a). The Urbach energy analysis confirms a well-ordered crystalline lattice with minimal band tailing and defect-mediated sub-gap states, further supporting the presence of clean, trap-free recombination channels in the solid state.

Additionally, the PL response is excitation-dependent, with the emission wavelength shifting as the excitation energy changes. This behavior indicates the presence of multiple emissive states and relaxation pathways, commonly observed in low-dimensional bismuth-based hybrids. The underlying mechanism is attributed to self-trapped excitons (STEs) formed within the distorted  $[Bi_2Br_{10}]^{4-}$  subunits. In such systems, the energy landscape contains shallow and deep potential wells created by lattice distortions and local electronic inhomogeneities, allowing excitons to relax into different emissive channels depending on the excitation energy. The indirect nature of the bandgap further supports phonon-assisted recombination, increasing spectral sensitivity to excitation conditions. Additionally, weak energetic disorder and dynamic coupling between the flexible organic cations and the inorganic framework contribute to the excitation-dependent tunability, as reflected in the shift of emission maxima.

The difference between the bandgap values extracted from liquid-phase UV-vis measurements (3.086 eV, Fig. 6) and solid-state DRS (2.9 eV, Fig. 10) is attributed to solvation effects, molecular rearrangements, and enhanced intermolecular interactions in the crystalline phase. Solvent screening in solution typically leads to an overestimation of the bandgap due to weaker exciton binding and limited inter-framework coupling, whereas solid-state measurements better reflect the condensed, polarizable environment. Furthermore, TD-DFT calculations (Fig. 17) yield a bandgap of 2.85 eV, closely matching the DRS-derived value, and confirming the indirect nature of the transition.

Finally, the strong correlation between the observed PL features and optical constants, including the penetration depth (Fig. 13) and extinction coefficient (Fig. 14), confirms the consistency of the material's optical behavior across techniques. The compound's broad absorption, strong Stokes shift, and stable emission make it a promising candidate for near-infrared emitters, broadband photonic absorbers, and hybrid optoelectronic devices where emission tunability and structural robustness are essential.





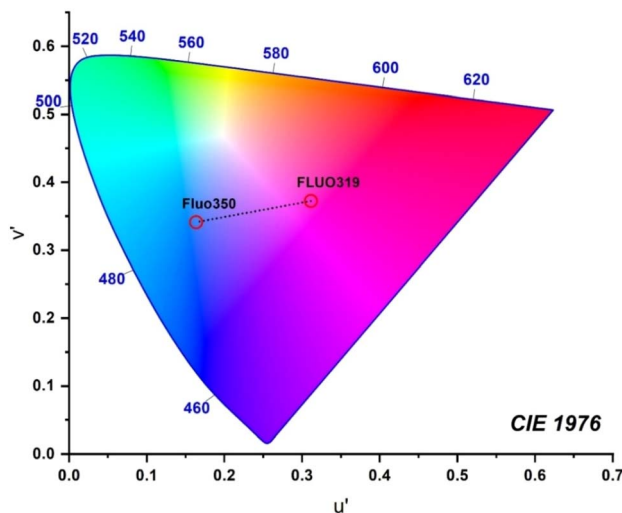


Fig. 9 Chromaticity diagram of  $(\text{C}_8\text{H}_{14}\text{N}_2)_2[\text{Bi}_2\text{Br}_{10}] \cdot 2\text{H}_2\text{O}$ .

Fig. 9 presents the CIE 1976 chromaticity diagram, offering a precise assessment of the emission color properties of  $(\text{C}_8\text{H}_{14}\text{N}_2)_2[\text{Bi}_2\text{Br}_{10}] \cdot 2\text{H}_2\text{O}$ . This diagram quantitatively represents the compound's photoluminescence (PL) emission in the perceptible color space, highlighting its potential for optoelectronic applications, such as LEDs, laser technologies, and displays. The CIE 1976 ( $u'$ ,  $v'$ ) color space ensures a perceptually uniform color distribution, making it the preferred standard for accurate evaluation of chromatic coordinates and emission purity. The diagram reveals two distinct ( $u'$ ,  $v'$ ) coordinates for two excitation wavelengths: 319 nm and 350 nm, correlating with the primary PL emission features observed in Fig. 8. The emission under 319 nm excitation is characterized by ( $u' = 0.311$ ,  $v' = 0.371$ ), placing it in the rose region, while under 350 nm excitation, the coordinates shift to ( $u' = 0.164$ ,  $v' =$

0.344), moving toward the blue-cyan region. This shift highlights a variation in emission behavior depending on excitation energy, linked to differences in radiative recombination pathways and electronic states within the band structure. A key feature of the chromaticity data is its correlation with the PL spectrum, particularly the transformation from a broad 645 nm peak to a sharp 706 nm peak, marking the deep-red emission region. The chromaticity coordinates reinforce the indirect bandgap nature of the material, as phonon-assisted recombination mechanisms lead to longer-wavelength emissions with defined spectral characteristics. The excitation-dependent emission suggests multiple relaxation pathways, likely influenced by exciton localization effects in the  $[\text{Bi}_2\text{Br}_{10}]^{4-}$  sublattices.

The narrow spread of chromaticity coordinates indicates a low density of defect states, minimizing non-radiative recombination losses, aligning with the low Urbach energy values (Fig. 12(a)). Additionally, the optical penetration depth (Fig. 13) and extinction coefficient variations (Fig. 14) confirm the efficient light absorption and emission within a well-defined spectral range, demonstrating excitation-dependent tunability and reinforcing its suitability for photonic applications, such as tunable LED phosphors, near-infrared emitters, and high-efficiency displays.

**3.3.2 Diffuse reflectance spectroscopy (DRS).** DRS is particularly valuable for materials exhibiting strong scattering effects, like polycrystalline solids and powdered samples, as it accurately estimates the optical bandgap by analyzing the reflectance profile and converting it to an absorption-like spectrum using the Kubelka-Munk function. Unlike liquid-state UV-vis (Fig. 6), which probes electronic transitions in solution, DRS provides a more precise bandgap determination in the condensed phase, where intermolecular interactions and lattice effects are significant. Fig. 10(a) and (b) present the DRS spectrum and absorption spectrum with derivative analysis,

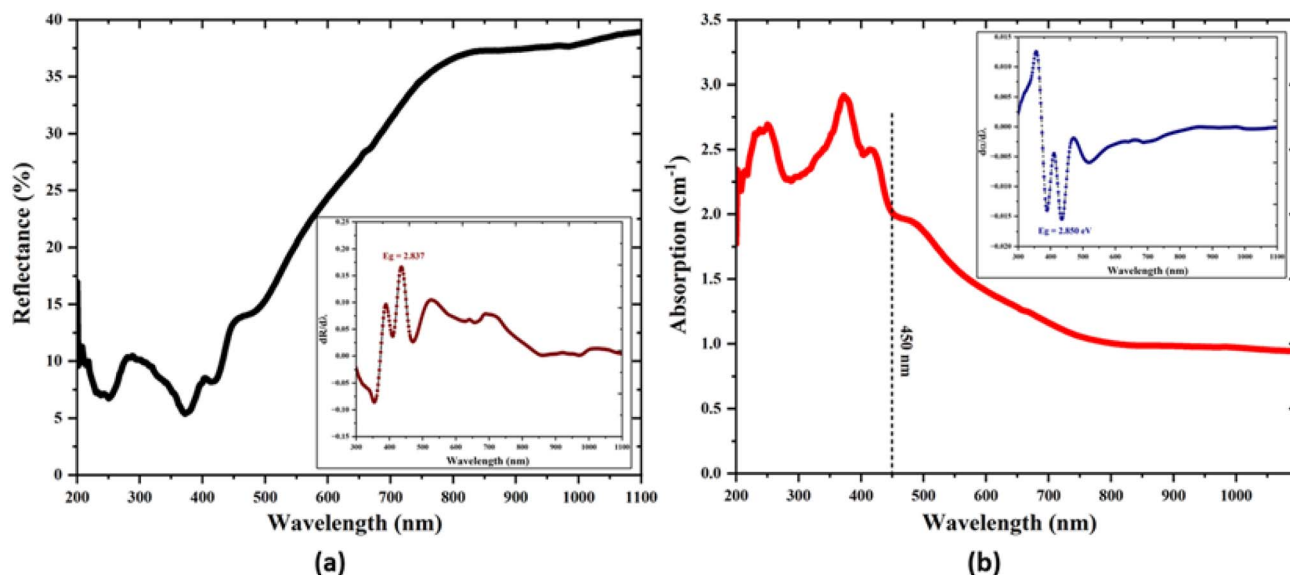


Fig. 10 (a) Diffuse Reflectance and (b) absorption spectra, (inset: derivatives).



offering a detailed evaluation of the solid-state optical properties of  $(C_8H_{14}N_2)_2[Bi_2Br_{10}] \cdot 2H_2O$ .

The DRS spectrum (Fig. 10(a)) shows a gradual reflectance decrease from the UV to visible region, with a well-defined edge around 400 nm (Fig. 10(b)), indicating strong absorption onset due to interband electronic transitions. Converting reflectance to an absorption spectrum reveals a pronounced band in the UV region, confirming charge-transfer excitations. The derivative analysis clarifies the absorption edge at 400 nm, suggesting that  $(C_8H_{14}N_2)_2[Bi_2Br_{10}] \cdot 2H_2O$  behaves as a semiconductor, absorbing UV and near-visible photons.

The optical bandgap extracted *via* the Tauc plot method (Fig. 11) confirms an indirect transition with  $E_g \approx 2.9$  eV, in agreement with DOS calculations (Fig. 17), which predict  $E_g = 2.85$  eV. The discrepancy with the liquid-state bandgap (3.086 eV, Fig. 6) highlights the effects of solid-state interactions, where molecular orbital overlap and crystal packing lead to a narrower bandgap compared to the solvated environment. This is corroborated by PL analysis (Fig. 8), where a broad 645 nm emission evolves into a sharp 706 nm peak, confirming an indirect band structure with phonon-assisted recombination. The DOS and PDOS (Fig. 17) reveal that the valence band maximum (VBM) is composed mainly of Br 4p states, with contributions from Bi 6p orbitals, while the conduction band minimum (CBM) consists of N 2p and C 2p states. The HOMO–LUMO transition involves intermolecular charge transfer from the Bi 6p + Br 4p orbitals to N 2p + C 2p orbitals, aligning with the solid-state absorption spectrum (Fig. 10(b)) and liquid-state UV-vis data (Fig. 8). This confirms the complex light absorption process in this system. The experimental absorption spectrum shows several distinct peaks, notably at 249 nm (4.98 eV), 371 nm (3.34 eV), 417 nm (2.97 eV), and 483 nm (2.57 eV), each corresponding to different types of electronic transitions. The 249 nm peak is primarily attributed to localized electronic excitations within the inorganic  $[Bi_2Br_{10}]^{4-}$  lattice, given its correspondence with the expected energy range of such

transitions in bismuth halide frameworks. However, since  $\pi$ – $\pi^*$  transitions in aromatic organic systems also typically occur in the 200–300 nm range, a partial spectral overlap with the organic cation cannot be definitively excluded. Making the 249 nm band arise predominantly from inorganic-centered excitations, with possible minor contributions from  $\pi$ – $\pi^*$  transitions within the organic component, consistent with the hybrid nature of the material and the potential for orbital coupling at higher excitation energies. The 371 nm peak corresponds to a charge transfer within the inorganic framework. The 417 nm peak represents intermolecular charge transfer (ICT), confirming strong coupling between the organic and inorganic components. The 483 nm peak suggests phonon-assisted transitions typical of indirect bandgap semiconductors, supporting the indirect bandgap nature confirmed by Tauc analysis (Fig. 11(a)) and DOS calculations (Fig. 17(a)). Overall, Fig. 10(a) and (b) provide a comprehensive understanding of the solid-state optical behavior of  $(C_8H_{14}N_2)_2[Bi_2Br_{10}] \cdot 2H_2O$ , reaffirming its indirect bandgap nature, strong UV absorption, and potential for optoelectronic applications. The integration of reflectance, absorption analysis, derivative spectral features, DOS calculations, and PL studies highlights its suitability for advanced photonic applications with precise bandgap control and efficient absorption.

Fig. 11 provides a detailed evaluation of the optical bandgap and transition nature in  $(C_8H_{14}N_2)_2[Bi_2Br_{10}] \cdot 2H_2O$ , essential for understanding its fundamental electronic properties. Fig. 11(a) presents the Tauc plots for direct and indirect transitions, where a clear linear extrapolation in the Kubelka–Munk plot confirms the indirect nature of the bandgap, yielding an  $E_g$  value of 2.9 eV. This result is consistent with the Density of States (DOS) calculations (Fig. 17(a)), which predict  $E_g = 2.85$  eV, further reinforcing the material's indirect band structure. The insets in Fig. 10(a) and (b), showing the derivatives of the reflectance and absorption spectra, provide an initial approximation of the bandgap at  $\sim 3.0$  eV, offering an

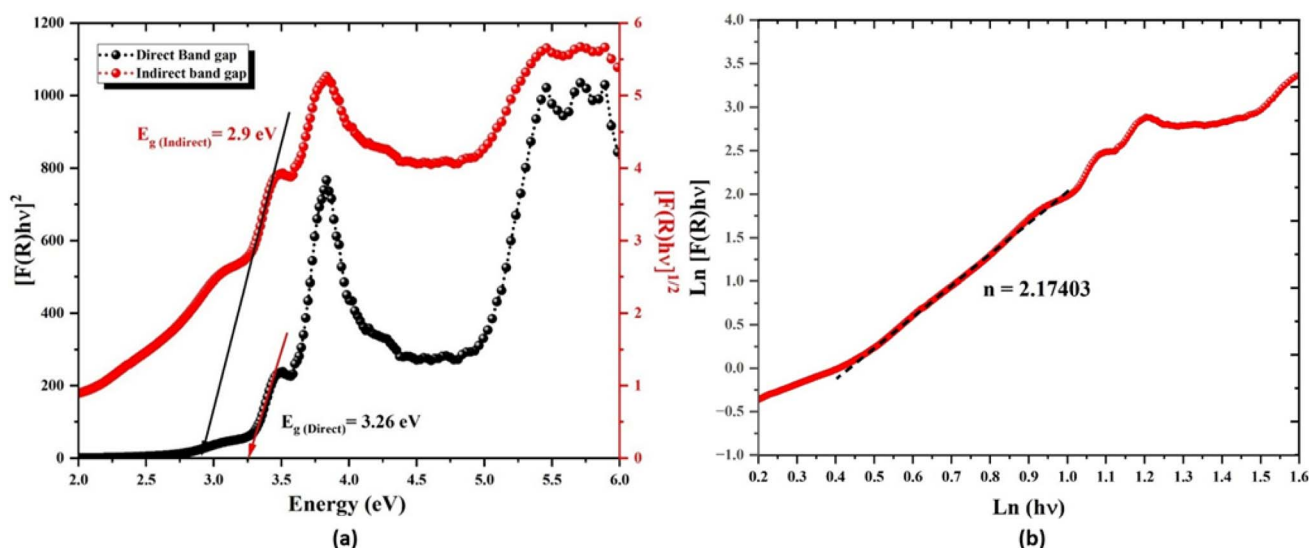


Fig. 11 (a) Direct versus indirect band gap determination *via* Tauc plot, and (b)  $\ln(\alpha hv)$  vs.  $\ln(hv - E_g)$  Plot.



independent confirmation of the absorption edge position before precise Kubelka–Munk's Tauc extrapolation. The Kubelka–Munk function is defined as follows:<sup>50,51</sup>

$$F(R) = \frac{K}{S} = \frac{(1 - R_\infty)^2}{2R_\infty}$$

According to inter-band absorption theory, the absorption coefficient near the threshold, in relation to incident energy, can be described by the following equation:<sup>52,53</sup>

$$\left[ \frac{F(R)h\nu}{t} \right]^{\frac{1}{n}} = A(h\nu - E_g)$$

where the thickness of the holder, denoted as  $t$ , is 1 mm.

Fig. 11(b) presents the  $\ln(F(R)h\nu)$  vs.  $\ln(h\nu - E_g)$  plot, which determines the exponent  $n$  in the Kubelka–Munk function, a critical parameter for identifying whether the transition is allowed direct ( $n = \frac{1}{2}$ ), allowed indirect ( $n = 2$ ), forbidden direct ( $n = 2/3$ ), or forbidden indirect ( $n = 3$ ). The best linear fit to the experimental data confirms  $n \approx 2$ , definitively proving that the bandgap is of an indirect allowed nature, aligning perfectly with the Stokes shift and phonon-assisted recombination processes observed in the PL spectrum (Fig. 8). The indirect nature is also evident in the continuous absorption behavior beyond the band edge in Fig. 10(b), particularly in the small peak at 483 nm, which is characteristic of indirect semiconductors where absorption extends beyond the main threshold due to phonon contributions.

The consistency between the DRS-derived bandgap (Fig. 11(a)), DOS calculations (Fig. 17(a)), PL characteristics (Fig. 8), and indirect transition coefficient (Fig. 11(b)) firmly establishes that  $(\text{C}_8\text{H}_{14}\text{N}_2)_2[\text{Bi}_2\text{Br}_{10}]\cdot 2\text{H}_2\text{O}$  is a semiconductor with an indirect bandgap, a crucial distinction that influences its charge carrier dynamics, exciton lifetime, and optoelectronic efficiency. These findings reinforce the material's potential for

photonic applications, where controlled bandgap engineering and minimal defect-induced electronic disorder are required for high-performance device integration.

**3.3.3 Determination of Urbach energy and threshold wavelength.** Fig. 12 provides critical insights into the electronic disorder and optical absorption characteristics of  $(\text{C}_8\text{H}_{14}\text{N}_2)_2[\text{Bi}_2\text{Br}_{10}]\cdot 2\text{H}_2\text{O}$ , essential for understanding its structural quality and light penetration properties.

Fig. 12(a) presents the Urbach energy ( $E_u$ ), which quantifies band tail states due to structural disorder, defects, or electron–phonon interactions. A low  $E_u$  indicates minimal disorder and a sharp absorption edge, as observed in Fig. 10(a) and (b), aligning with the absence of mid-gap states in the DOS spectrum (Fig. 17(a)). This confirms the material's high electronic stability and supports the indirect nature of the bandgap, as indirect semiconductors typically show extended absorption tails due to phonon-assisted transitions. Fig. 12(b) shows the evolution of  $(\alpha/\lambda)^2$  with  $1/\lambda$ , revealing how the absorption coefficient varies with wavelength. The trend, correlating with the diffuse reflectance data (Fig. 10(a)) and extinction coefficient (Fig. 14), suggests uniform light absorption across energy ranges, indicating high crystallinity and purity. This smooth, continuous increase in  $(\alpha/\lambda)^2$  further validates the calculated bandgap. The combination of low Urbach energy (Fig. 12(a)), defined absorption characteristics (Fig. 12(b)), and band structure analysis (Fig. 11(a) and (b)) confirms that  $(\text{C}_8\text{H}_{14}\text{N}_2)_2[\text{Bi}_2\text{Br}_{10}]\cdot 2\text{H}_2\text{O}$  has a stable electronic structure with minimal defect-induced recombination losses, making it suitable for optoelectronic applications requiring strong light absorption and controlled charge carrier dynamics.

**3.3.4 Penetration depth and optical extinction.** Fig. 13 and 14 evaluate the material's light interaction properties, specifically penetration depth ( $\delta$ ) and extinction coefficient ( $K$ ), essential for understanding optical absorption and energy dissipation in  $(\text{C}_8\text{H}_{14}\text{N}_2)_2[\text{Bi}_2\text{Br}_{10}]\cdot 2\text{H}_2\text{O}$ .

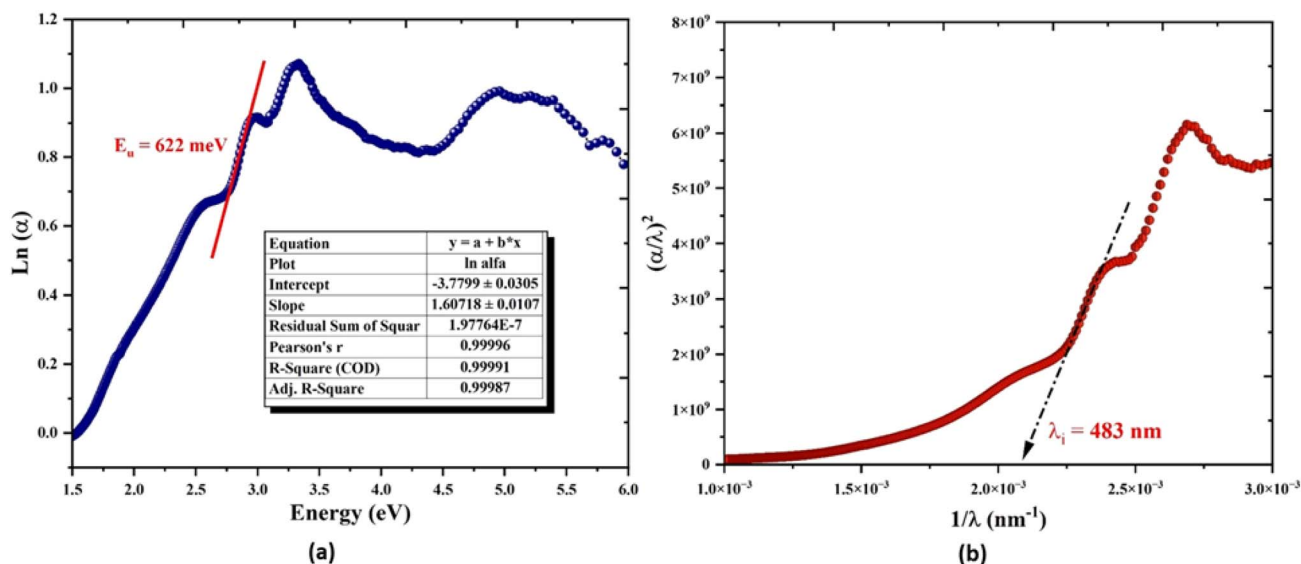


Fig. 12 (a) Urbach energy analysis, and (b) evolution of the  $(\alpha/\lambda)^2$  curve as a function of  $1/\lambda$ .



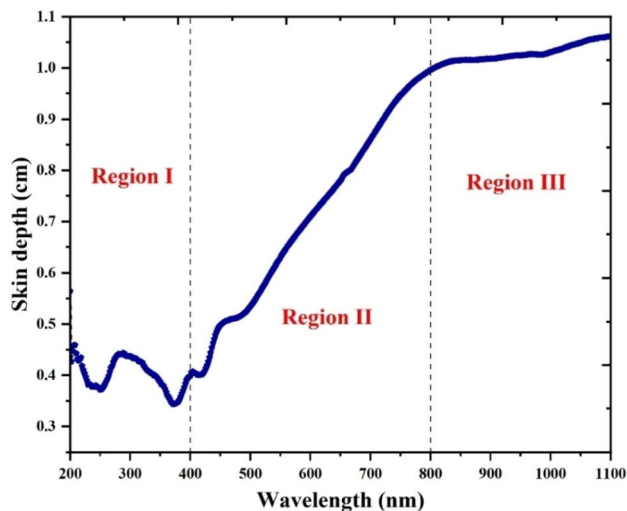


Fig. 13 Variation of penetration depth ( $\delta$ ) with wavelength ( $\lambda$ ).

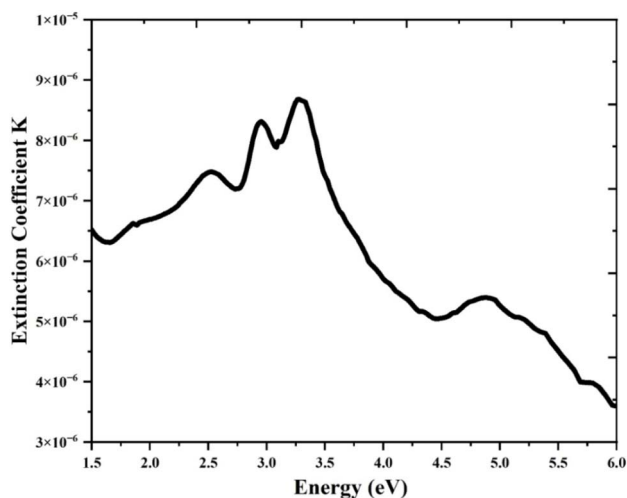


Fig. 14 Variation of extinction coefficient ( $K$ ) as a function of wavelength.

Fig. 13 illustrates the penetration depth vs.  $\lambda$ , given by the formula:<sup>54</sup>

$$\delta(\lambda) = \frac{1}{\alpha(\lambda)}$$

The plot shows three distinct regions:

High-energy UV region ( $\lambda < 400$  nm) – Minimal penetration depth due to strong absorption from high-energy charge transfer transitions, consistent with the 249 nm absorption peak (Fig. 10(b)).

Mid-visible region (400–800 nm) – increased  $\delta$ , indicating reduced absorption and stronger light penetration, typical of indirect semiconductors.

Near-infrared region ( $\lambda > 800$  nm) – further increase in  $\delta$ , confirming weaker absorption and the absence of mid-gap defect states (Fig. 17(a), DOS analysis).

Fig. 14 shows the optical extinction coefficient ( $K$ ), derived from:<sup>55</sup>

$$K(\lambda) = \frac{\lambda \alpha(\lambda)}{4\pi}$$

Four peaks are identified: 253 nm, 379 nm, 420 nm, and 492 nm. The 253 nm peak corresponds to high-energy charge transfer transitions in the inorganic framework, while the 379 nm and 420 nm peaks reflect intramolecular charge transfer (ICT) between the organic and inorganic sublattices. The 492 nm peak aligns with the continuous absorption tail, confirming phonon-assisted transitions characteristic of indirect semiconductors. The correlation between penetration depth, extinction coefficient, and absorption spectrum establishes  $(\text{C}_8\text{H}_{14}\text{N}_2)_2[\text{Bi}_2\text{Br}_{10}] \cdot 2\text{H}_2\text{O}$  as a material with well-defined absorption, minimal optical losses, and efficient charge transfer, making it ideal for photonic and optoelectronic applications requiring precise light-matter interaction control.

**3.3.5 Evolution of the refractive index and optical conductivity analysis.** Fig. 15 and 16 provide crucial insights into the optical response and electronic transport properties of  $(\text{C}_8\text{H}_{14}\text{N}_2)_2[\text{Bi}_2\text{Br}_{10}] \cdot 2\text{H}_2\text{O}$ , focusing on the refractive index ( $n$ ) and optical conductivity ( $\sigma_{\text{opt}}$ ), which are fundamental for assessing its performance in waveguides, optoelectronic devices, and photonic applications. The optical refractive index  $n$  change can be expressed by the following equation:<sup>56</sup>

$$n(\lambda) = \frac{1 + R + \sqrt{4R - (1 - R)^2 K^2}}{1 - R} = \frac{1 + R}{1 - R} + \sqrt{\frac{4R}{(1 - R)^2} - K^2}$$

Fig. 15 illustrates the variation of the refractive index ( $n$ ) as a function of wavelength across the 200–1100 nm range. Contrary to the classical dispersion behavior typically observed in simple inorganic materials, where  $n$  decreases monotonically with increasing wavelength, the present compound reveals a more complex and region-dependent evolution:

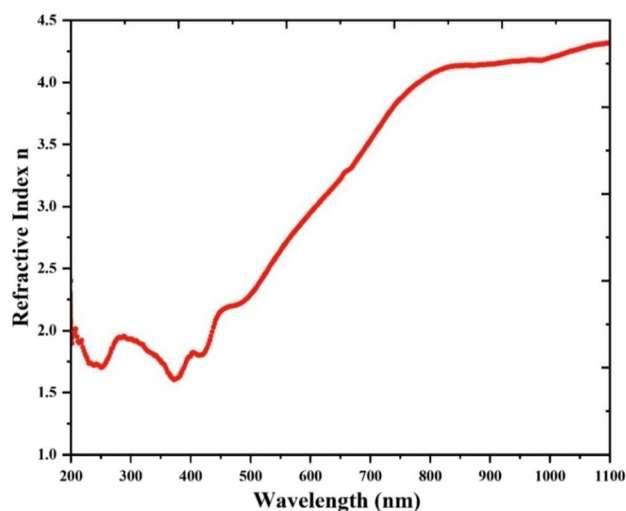


Fig. 15 Refractive index ( $n$ ) plot.





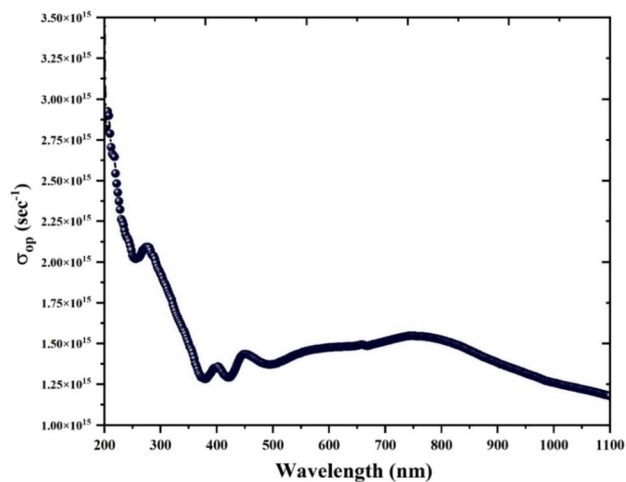


Fig. 16 Optical conductivity plot.

In the ultraviolet region ( $\lambda < 400$  nm),  $n$  remains relatively low ( $\sim 1.5$ – $2.0$ ), which can be attributed to the proximity of strong absorption edges and the influence of anomalous dispersion effects near the band edge.

Across the visible region (400–800 nm),  $n$  increases progressively and more markedly, reflecting enhanced electronic polarization processes and charge-transfer interactions within the hybrid inorganic–organic network.

In the near-infrared region ( $\lambda > 800$  nm), the rise of  $n$  continues but at a diminished rate, with values approaching and slightly exceeding 4.0. This saturation-like behavior is indicative of a high dielectric response combined with minimal absorption losses, underscoring the stability of the optical response at longer wavelengths.

Such non-classical dispersion characteristics are emblematic of bismuth-based organic–inorganic hybrid materials, where the unusually strong polarizability of  $\text{Bi}^{3+}$  cations, the stereochemically active  $6s^2$  lone pairs, and the cooperative electronic coupling between organic and inorganic substructures contribute synergistically to complex optical responses. Overall, this distinctive dispersion profile confirms both the strong optical anisotropy and dense electronic structure of the compound, in line with the high polarizability and the indirect band gap nature previously established by DOS and optical analyses.

The optical conductivity  $\sigma_{\text{opt}}$  can be calculated using the following expression where  $c$  is the speed of light in free space:

$$\sigma_{\text{op}} = \frac{\alpha(\lambda)n(\lambda)c}{4\pi k_e(\lambda)}$$

Fig. 16 presents the optical conductivity ( $\sigma_{\text{opt}}$ ), a key parameter reflecting the material's ability to absorb and transfer photogenerated charge carriers, with four key peaks at 275 nm, 398 nm, 447 nm, and 784 nm. The 275 nm peak corresponds to high-energy charge transfer excitations, while the 398 nm and 447 nm peaks align with ICT processes between the inorganic and organic components, reinforcing the hybrid

nature of the electronic transitions. The 784 nm peak, appearing in the near-IR region, suggests long-wavelength residual absorption, likely due to defect-mediated transitions or phonon interactions, a feature common in indirect bandgap semiconductors.

The consistency between the refractive index trends, optical conductivity peaks, and band structure analysis (Fig. 16 and 17(a)) underscores the material's well-defined electronic transitions, low defect density, and high potential for optoelectronic applications requiring precise control over refractive and conductive properties.

The compound  $(\text{C}_8\text{H}_{14}\text{N}_2)_2[\text{Bi}_2\text{Br}_{10}] \cdot 2\text{H}_2\text{O}$  exhibits markedly distinct optical properties compared to the recently reported antimony-based hybrid  $(\text{C}_8\text{H}_{14}\text{N}_2)_2[\text{Sb}_2\text{I}_{10}] \cdot 2\text{H}_2\text{O}$ ,<sup>57</sup> despite both adopting dimeric  $[\text{M}_2\text{X}_{10}]^{4-}$  structural motifs. While both structures feature edge-sharing halometalate dimers stabilized by the same organic cation, the substitution of  $\text{Sb}^{3+}$  with  $\text{Bi}^{3+}$  and the use of  $\text{Br}^-$  instead of  $\text{I}^-$  lead to significantly different electronic environments and resulting optical behavior. Our bismuth-based compound demonstrates a much narrower band gap (2.9 eV) compared to the wide-gap antimony analog (5.27 eV), shifting absorption from the ultraviolet into the visible region. This enhancement is attributed to the stronger spin–orbit coupling (SOC) effects associated with the heavier  $\text{Bi}^{3+}$  center, which effectively reduce the band gap by stabilizing the conduction band minimum. Furthermore, the use of bromide (a harder halide than iodide) contributes to increased

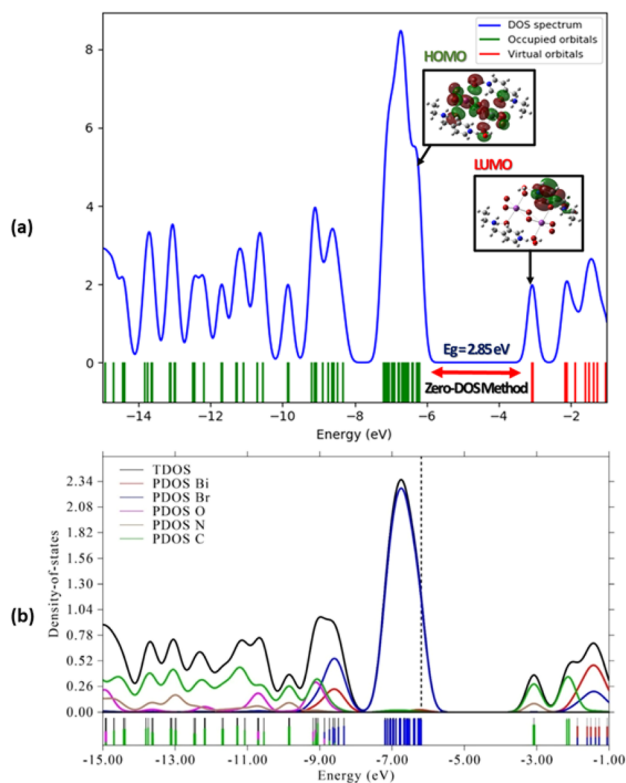


Fig. 17 (a) Total density of state (DOS), and (b) partial density of state (PDOS) spectra of the compound spectrum and the frontier molecular orbitals of the compound.



orbital overlap and a more delocalized electronic structure. These differences translate into more favorable optical characteristics for visible-light-driven applications in our compound, including enhanced light-harvesting capability and emission behavior, as confirmed by PL and TD-DFT analyses.

### 3.4. Theoretical investigation

**3.4.1 Frontier molecular orbital (FMO) analysis.** The analysis of Frontier Molecular Orbitals (FMOs) provides insights into the compound's electronic, optical, and chemical reactivity. The Highest Occupied Molecular Orbital (HOMO) indicates the electron-donating ability, while the Lowest Unoccupied Molecular Orbital (LUMO) represents its electron-accepting capacity. The HOMO–LUMO gap reflects molecular stability and reactivity, with a wider gap suggesting lower reactivity and a narrower gap indicating higher reactivity. Ionization energy ( $E_i$ ) is the negative value of  $E_{(\text{HOMO})}$ , and electron affinity ( $E_A$ ) is the negative value of  $E_{(\text{LUMO})}$ . Electronegativity ( $\chi$ ), global hardness ( $\eta$ ), softness ( $S$ ), and electrophilicity index ( $\omega$ ) can be derived using specific formulas, with  $\mu$  representing the electronic chemical potential ( $\mu = \frac{1}{2}(E_{(\text{LUMO})} + E_{(\text{HOMO})})$ ). Fig. 20.S(a) shows the HOMO and LUMO orbitals' distribution, with energy values and calculated parameters like band gap, hardness, and softness presented in Table 4.S. DFT calculations using the B3LYP functional and the LanL2DZ basis set were performed, along with time-dependent DFT (TD-DFT) in water for electronic absorption analysis. Fig. 4.S shows the simulated UV-vis spectrum, with major electronic transitions listed in Table 5.S. The second transition dominates the spectrum, while Fig. 5.S reveals the 336 nm absorption peak corresponding to a HOMO-to-LUMO charge transfer transition. Here, the HOMO electrons are localized on the inorganic dimer (bismuth and bromide atoms), while the LUMO is over the  $\pi$ -system of the organic cation. This transition contributes 88% to the absorption. Additional peaks at 332 nm and 330 nm arise from excitations involving orbitals H-2, H-1, and H-3 to the LUMO, with contributions of 76%, 87%, and 15%, respectively. The electrons are localized on the bromide orbitals, leading to  $\pi$ – $\pi^*$  transitions. The calculated HOMO–LUMO gap of 2.85 eV closely matches the experimental band gap of 2.9 eV, confirming the consistency of the theoretical and experimental results.

**3.4.2 MEP, NCI-RDG, ELF, and LOL analyses.** The combination of Molecular Electrostatic Potential (MEP), Non-Covalent Interaction Reduced Density Gradient (NCI-RDG), Electron Localization Function (ELF), and Localized Orbital Locator (LOL) analyses provides insights into the electronic structure and intermolecular interactions in hybrid materials. These DFT-based methods reveal charge distribution, non-covalent bonding, and electron localization, essential for understanding the stability and functionality of organic–inorganic systems. MEP highlights electrophilic and nucleophilic regions, identifying interaction sites, while NCI-RDG maps weak forces like hydrogen bonding and van der Waals interactions, revealing supramolecular organization. ELF and LOL offer complementary views on electron localization and orbital interactions, illuminating the bonding nature and reactivity.

Together, these analyses connect theoretical predictions with experimental data, facilitating the design of hybrid materials with optimized properties. The following sections detail these calculations for  $(\text{C}_8\text{H}_{14}\text{N}_2)_2[\text{Bi}_2\text{Br}_{10}]\cdot 2\text{H}_2\text{O}$ , focusing on charge distribution, bonding, and electronic interactions critical to its structure and functionality.

#### 3.4.3 Molecular electrostatic potential MEP analysis.

Fig. 6.S shows the molecular electrostatic potential (MEP) surface for  $(\text{C}_8\text{H}_{14}\text{N}_2)_2[\text{Bi}_2\text{Br}_{10}]\cdot 2\text{H}_2\text{O}$ , revealing charge distribution and potential interaction sites. Red regions (negative electrostatic potential) around the bromide ligands in  $[\text{Bi}_2\text{Br}_{10}]^{2-}$  indicate electron-rich sites, suggesting these bromides act as hydrogen bond acceptors with water molecules or the organic cations. Blue regions (positive potential) around the protonated nitrogen atoms of the organic cations highlight hydrogen bond donor sites. The MEP plot underscores the polar nature of the compound, with charge separation between the cationic and anionic components. The protonated organic cations exhibit electrophilic sites (blue), which may stabilize the crystal through hydrogen bonding. Negative potential on the bromides in the anionic cluster confirms ionic interactions between the cations and anions. Neutral zones (white) indicate nonpolar interactions or steric hindrance. Water molecules introduce additional hydrogen bonding sites, enhancing structural stability and influencing thermal and solubility properties. The MEP also highlights reactivity, with electron-rich bromides suggesting susceptibility to electrophilic attack, while the electron-deficient organic cations may act as nucleophilic sites. The uniform charge distribution indicates a well-organized crystal lattice, with complementary electronic profiles between the organic and inorganic components.

**3.4.4 Non-covalent interaction NCI-RDG analysis.** Fig. 7.S presents the Non-Covalent Interaction (NCI) visualization (a) and Reduced Density Gradient (RDG) plot (b) for  $(\text{C}_8\text{H}_{14}\text{N}_2)_2[\text{Bi}_2\text{Br}_{10}]\cdot 2\text{H}_2\text{O}$ , offering insights into weak interactions crucial for the compound's stability. The NCI isosurface (Fig. 7.S(a)) shows green surfaces representing van der Waals interactions, blue regions for strong hydrogen bonds, and red regions indicating repulsive interactions, particularly around the bulky  $[\text{Bi}_2\text{Br}_{10}]^{2-}$  units. This distribution highlights the balance of stabilizing and destabilizing forces within the crystal lattice.

The RDG scatter plot (Fig. 7.S(b)) quantifies these interactions: blue peaks for attractive hydrogen bonds, green for van der Waals, and red for steric repulsions. The sharp blue peaks confirm dominant hydrogen bonding between the organic cation and the anionic framework, while green peaks show van der Waals interactions, and red peaks reflect steric repulsions.

These visualizations reveal the synergy of hydrogen bonding, van der Waals forces, and steric effects in stabilizing the hybrid framework. Understanding these interactions is crucial for designing materials with optimized properties for catalysis, sensing, or optoelectronics.

**3.4.5 Electron localization function (ELF) and localized orbital locator (LOL) analyses.** Fig. 8.S illustrates the theoretical formula unit of the hybrid compound  $(\text{C}_8\text{H}_{14}\text{N}_2)_2[\text{Bi}_2\text{Br}_{10}]\cdot 2\text{H}_2\text{O}$ , displayed across three principal planes: (XY), (XZ), and (YZ). This multi-planar representation offers a comprehensive



geometric framework for interpreting the spatial arrangement of atoms, bond angles, and intermolecular interactions. These orientations establish the structural basis for the subsequent electronic topological analyses shown in Fig. 9.S and 10.S.

Fig. 9.S displays the Electron Localization Function (ELF) mapped across the same three planes, highlighting regions of high electron localization ( $\text{ELF} \approx 1.0$ , red) corresponding to lone pairs and covalent bonds, and regions of delocalization ( $\text{ELF} \approx 0.0$ , blue) indicative of weak interactions. In the (XY) plane, symmetric electron localization is observed around the Bi–Br bonds, with pronounced lone pair density on  $\text{Bi}^{3+}$  centers. The (XZ) and (YZ) planes further emphasize electron-rich regions associated with hydrogen bonding between the halides and coordinated water molecules. These features collectively confirm a mixed bonding character dominated by localized covalent and noncovalent interactions.

Fig. 10.S complements this with Localized Orbital Locator (LOL) maps in the same spatial planes. The 3D surface plots reveal peaks in electron pairing near key bonding sites, while the 2D contour maps highlight anisotropic orbital localization, transitioning from low (blue) to high (red) values. The (XY) plane demonstrates strong localization along covalent Bi–Br bonds, whereas the (XZ) and (YZ) views reinforce the directional nature of electron density across the inorganic dimer and organic interface. Together, ELF and LOL analyses provide consistent and detailed insight into the electronic distribution and bonding topology of the hybrid, underscoring the structural and electronic coherence of the system.

### 3.5. Hirshfeld surface analysis (HSA)

A Hirshfeld surface analysis of the compound was performed using CrystalExplorer to examine intermolecular interactions, with 2D fingerprint plots providing a quantitative assessment. Fig. 11.S presents 3D Hirshfeld surface representations of the molecule, mapped over different functions: (a) normalized  $d_{\text{norm}}$ , (b) shape index, and (c) curviness. The surface is color-coded, where red regions denote areas with the strongest interaction contributions, blue regions indicate minimal contributions, and white regions show non-contributory points. In Fig. 11.S(a), pronounced red depressions on the surface highlight the proximity of hydrogen bond donors and acceptors, particularly near  $\text{H}_2\text{O}$  molecules and Br atoms within the inorganic framework. These interactions confirm the presence of  $\text{N}\cdots\text{H}\cdots\text{Br}$ ,  $\text{N}\cdots\text{H}\cdots\text{O}$ , and  $\text{O}\cdots\text{H}\cdots\text{Br}$  hydrogen bonds, which are vital for maintaining the structure. White regions are indicative of H/H contacts, which play a significant role in molecular packing. The shape index function in Fig. 11.S(b) provides insight into  $\pi$ – $\pi$  stacking interactions, displaying alternating red and blue triangular regions. The absence of adjacent triangular features indicates the lack of  $\pi$ – $\pi$  interactions in this compound. The curviness map shown in Fig. 11.S(c) highlights areas of significant surface curvature, which help identify molecular contact regions and assess the coordination environment within the crystal structure.

Fig. 12.S illustrates the 2D fingerprint plots, offering a comprehensive representation of total contacts contributing

to the Hirshfeld surface. The plot spans a distance range of 0.6 to 2.8 Å, with  $d_{\text{e}}$  and  $d_{\text{i}}$  values plotted along respective axes. The analysis reveals that the dominant interaction is  $\text{H}\cdots\text{Br}$  (57.6% of the total surface contacts), with  $\text{H}\cdots\text{H}$  contacts contributing 22.5%. The prevalence of hydrogen bonding interactions indicates their importance in the material's stability, impacting its mechanical, thermal, optical, and conductive properties.

Additionally, an assessment of crystal voids was performed to gain insights into packing efficiency and the physicochemical properties of the material. Crystal voids represent unoccupied regions in the solid structure, affecting solubility, density, mechanical strength, and thermal conductivity. These voids also facilitate molecular vibrations, influencing the compound's behavior. Using CrystalExplorer 21.5, the void volume was determined to be  $101.58 \text{ \AA}^3$ , representing 5.9% of the unit cell volume, as shown in Fig. 13.S. This suggests a high packing density, contributing to enhanced mechanical robustness and structural integrity. The reduced void space minimizes defect sites, preventing crack formation and propagation, while also improving thermal conductivity by allowing better phonon transport. These properties indicate that the hybrid material is a promising candidate for applications requiring both high optical quality and mechanical stability.

## 4. Conclusion

This study presents the synthesis, structural characterization, vibrational properties, and optical behavior of the newly developed bismuth-based hybrid material  $(\text{C}_8\text{H}_{14}\text{N}_2)_2[\text{Bi}_2\text{Br}_{10}]\cdot 2\text{H}_2\text{O}$ . The single-crystal X-ray diffraction analysis confirmed its monoclinic  $P2_1/c$  structure, with edge-sharing  $[\text{Bi}_2\text{Br}_{10}]^{4-}$  dimeric units playing a key role in stabilizing the 3D hydrogen-bonded network. Hirshfeld surface analysis and 2D fingerprint plots revealed dominant  $\text{H}\cdots\text{Br}$  and  $\text{H}\cdots\text{H}$  interactions, highlighting the impact of non-covalent forces on the material's supramolecular architecture. The optical study demonstrated a strong correlation between experimental and theoretical findings, with UV-vis spectroscopy confirming an indirect band gap of 2.9 eV (solid-state) and 3.086 eV (solution), in agreement with DFT calculations. The photoluminescence (PL) spectrum revealed blue and rose emission and CIE chromaticity analysis confirmed well-defined emission properties, making this material suitable for light-emitting and optoelectronic applications. Furthermore, DFT-based electronic structure analysis, including ELF, LOL, RDG, and NCI calculations, provided crucial insights into charge localization, electron delocalization, and weak interaction contributions within the hybrid lattice. These findings emphasize the material's stability, charge transport behavior, and potential for luminescent applications. With its well-defined band gap and strong luminescent response,  $(\text{C}_8\text{H}_{14}\text{N}_2)_2[\text{Bi}_2\text{Br}_{10}]\cdot 2\text{H}_2\text{O}$  stands out as a promising candidate for optoelectronic devices, photonic applications, and next-generation luminescent materials. Future work should focus on stability assessments, device integration, and tunability through chemical modifications to further optimize its functional properties.



The molecular architecture of  $(\text{C}_8\text{H}_{14}\text{N}_2)_2[\text{Bi}_2\text{Br}_{10}]\cdot 2\text{H}_2\text{O}$  exemplifies an acceptor–donor–acceptor (A–D–A) system, where the organic cations function as electron-rich donors and the bismuth bromide dimeric anion serves as a robust electron acceptor. This configuration facilitates effective charge transfer between the organic and inorganic sublattices, as supported by the observed optical transitions and electronic structure features. The properties uncovered, such as the indirect band gap, strong refractive response, and prominent charge transfer bands, are indicative of generalizable trends among low-dimensional bismuth-based hybrids. Substitution or structural modification of the donor units (*e.g.*, using more  $\pi$ -conjugated or electron-rich cations) or the inorganic acceptor (*via* halide tuning) offers a promising route to modulate the electronic and photophysical properties systematically. These findings highlight the compound's relevance within donor–acceptor materials design and suggest its potential utility as a model system for developing next-generation hybrid optoelectronic materials.

## Conflicts of interest

The authors declare that they have no known competing financial interests or personal relationships that could have appeared to influence the work reported in this paper.

## Data availability

The raw/processed data required to reproduce these findings are available and can be sent if requested.

CCDC 2384365 contains the supplementary crystallographic data for this paper.<sup>58</sup>

Supplementary information is available. See DOI: <https://doi.org/10.1039/d5ra06614j>.

## Acknowledgements

I sincerely thank Mrs Sameh DAMMAK, Principal Engineer of the Physics Department at the Faculty of Sciences, University of Sfax, for conducting the chemical analyses using FTIR and UV-visible spectroscopy.

## References

- 1 J. F. Scott, Applications of modern ferroelectrics, *Science*, 2007, **315**, 954–959.
- 2 S. T. Han, Y. Zhou and V. A. Roy, Towards the development of flexible non-volatile memories, *Adv. Mater.*, 2013, **25**, 5425–5449.
- 3 J. Li, J. Claude, L. E. Norena-Franco, S. I. Seok and Q. Wang, Electrical energy storage in ferroelectric polymer nanocomposites containing surface-functionalized BaTiO<sub>3</sub> nanoparticles, *Chem. Mater.*, 2008, **20**, 6304–6306.
- 4 A. W. Kelley, A. Nicholas, J. C. Ahern and B. Chan, *J. Alloys Compd.*, 2016, **670**, 337.
- 5 L.-M. Wu, X.-T. Wu and L. Chen, *Coord. Chem. Rev.*, 2012, **253**, 2787–2804.
- 6 N. Mercier, N. Louvain and W. H. Bi, *CrystEngComm*, 2009, **11**, 720–734.
- 7 B. Kulicka, T. Lis, V. Kinzhybalo, R. Jakubas and A. Piecha, *Polyhedron*, 2010, **29**, 2014–2022.
- 8 Y. Chen, Z. Yang, X.-Y. Wu, C.-Y. Ni, Z.-G. Ren, H.-F. Wang and J.-P. Lang, *Phys. Chem. Chem. Phys.*, 2011, **13**, 5659–5667.
- 9 A. Piecha, R. Jakubas, V. Kinzhybalo and W. Medycki, *J. Mol. Struct.*, 2012, **1013**, 55–60.
- 10 W. X. Chai, J. Lin, L. Song, L. S. Qin, H. S. Shi, J. Y. Guo and K. Y. Shu, *Solid State Sci.*, 2012, **14**, 1226–1232.
- 11 M. A. Tershansy, A. M. Goforth, J. R. Gardinier, M. D. Smith and L. Peterson, *Solid State Sci.*, 2007, **9**, 410–420.
- 12 C. Hrizi, A. Trigui, Y. Abid, N. Chniba-Boudjada, P. Bordet and S. Chaabouni, *J. Solid State Chem.*, 2011, **184**, 3336–3344.
- 13 A. Gabor, M. Weclawik, B. Bondzior and R. Jakubas, *CrystEngComm*, 2015, **27**, 3286.
- 14 R. G. Lin, G. Xu, G. Lu, M. S. Wang, P. X. Li and G. C. Guo, *Inorg. Chem.*, 2014, **53**, 5538–5545.
- 15 N. Leblanc, M. Allain, N. Mercier and L. Sanguinet, *Cryst. Growth Des.*, 2011, **11**, 2064–2069.
- 16 R. G. Lin, G. Xu, M. S. Wang, G. Lu, P. X. Li and G. C. Guo, *Inorg. Chem.*, 2013, **52**, 1199–1205.
- 17 Y.-J. Wang and L. Xu, *J. Mol. Struct.*, 2008, **875**, 570–576.
- 18 Y.-H. Peng and S.-F. Sun, *Inorg. Chem. Commun.*, 2012, **22**, 29–32.
- 19 Y.-H. Peng, S.-F. Sun, X.-H. Yang, T. Gao, Y. Li and J. Wang, *J. Mol. Struct.*, 2014, **1056–1057**, 202–208.
- 20 S. A. Adonin, M. N. Sokolov and V. P. Fedin, *Coord. Chem. Rev.*, 2016, **312**, 1–21.
- 21 L. Sobczyk, R. Jakubas and J. Zaleski, Self-assembly of Sb(III) and Bi(III) halo-coordinated octahedra in salts of organic cations: structure, properties, and phase transitions, *Pol. J. Chem.*, 1997, **71**, 265–300.
- 22 W. Zhang and R.-G. Xiong, Ferroelectric metal-organic frameworks, *Chem. Rev.*, 2012, **112**, 1163–1195.
- 23 O. V. Dolomanov, L. J. Bourhis, R. J. Gildea, J. A. K. Howard and H. Puschmann, Structural analysis using OLEX2, *J. Appl. Crystallogr.*, 2009, **42**, 339.
- 24 G. M. Sheldrick, Space-group determination study, *Acta Crystallogr., Sect. A*, 2015, **71**, 3.
- 25 G. M. Sheldrick, Crystal structure refinement, *Acta Crystallogr., Sect. C: Struct. Chem.*, 2015, **71**, 3.
- 26 K. Brandenburg, and H. Putz, *Diamond Crystal Analysis*, Crystal Impact GbR, Bonn, Germany, 1999.
- 27 L. Chęcinska, S. Grabowsky, M. Malecka, A. J. Rybarczyk-Pirek, A. Józwiak, C. Paulmann and P. Luger, Electron-density study, *Acta Crystallogr., Sect. B: Struct. Sci.*, 2011, **67**, 569.
- 28 S. K. Seth, D. Sarkar, A. D. Jana and T. Kar, Crystallographic and Hirshfeld analysis, *Cryst. Growth*, 2011, **11**, 4837.
- 29 S. K. Seth, I. Saha, C. Estarellas, A. Frontera, T. Kar and S. Mukhopadhyay, Self-assembly complexes study, *Cryst. Growth*, 2011, **11**, 3250.
- 30 S. K. Seth, D. Sarkar and T. Kar, Hydrogen-bonded supramolecular layers study, *CrystEngComm*, 2011, **13**, 4528.
- 31 S. K. Seth, D. Sarkar, A. Roy and T. Kar, Supramolecular self-assembly analysis, *CrystEngComm*, 2011, **13**, 6728.





- 32 S. K. Seth, N. C. Saha, S. Ghosh and T. Kar, Pyrazole derivative analysis, *Chem. Phys. Lett.*, 2011, **506**, 309.
- 33 S. K. Seth, P. C. Mandal, T. Kar and S. Mukhopadhyay, Oxo-bridged Fe(III) complex study, *J. Mol. Struct.*, 2011, **994**, 109.
- 34 P. Manna, S. K. Seth, A. Das, J. Hemming, R. Prendergast, M. Helliwell, S. R. Choudhury, A. Frontera and S. Mukhopadhyay, Anion- $\pi$  interaction analysis, *Inorg. Chem.*, 2012, **51**, 3557.
- 35 R. Spackman, M. J. Turner, J. J. McKinnon, S. K. Wolff, D. J. Grimwood, D. Jayatilaka and M. A. Spackman, Hirshfeld surface analysis using CrystalExplorer, *J. Appl. Crystallogr.*, 2021, **54**, 1006.
- 36 M. A. Spackman and J. J. McKinnon, Fingerprinting in crystal structures, *CrystEngComm*, 2002, **4**, 378.
- 37 J. J. McKinnon, M. A. Spackman and A. S. Mitchell, Tools for visualizing interactions in crystals, *Acta Crystallogr., Sect. B: Struct. Sci.*, 2004, **60**, 627.
- 38 S. K. Seth, G. C. Maity and T. Kar, Para-nitro benzylidene study, *J. Mol. Struct.*, 2011, **1000**, 120.
- 39 A. L. Rohl, M. Moret, W. Kaminsky, K. Claborn, J. J. McKinnon and B. Kahr, Crystallographic inadequacies study, *Cryst. Growth*, 2008, **8**, 4517.
- 40 J. J. McKinnon, D. Jayatilaka and M. A. Spackman, Quantitative analysis with Hirshfeld surfaces, *Chem. Commun.*, 2007, **37**, 3814.
- 41 A. Tounsi, S. Elleuch, B. Hamdi, R. Zouari and A. Ben Salah, Hybrid compound study, *J. Mol. Struct.*, 2017, **1141**, 512.
- 42 N. Zhanpelsov, M. Matsuoka, H. Yamashite and M. Anpo, NO molecule interaction study, *J. Phys. Chem. B*, 1998, **102**, 6915.
- 43 N. Niclasc, M. Dolg, H. Stoll and H. Preuss, Pseudopotential study of noble gases, *J. Chem. Phys.*, 1995, **102**, 8942.
- 44 M. J. Frisch, G. W. Trucks, and H. B. Schlegel, *Gaussian Program for Crystal Structure Determination*, Gaussian, Inc., Wallingford, CT, 2016.
- 45 R. Dennington, T. A. Keith, and J. M. Millam, *GaussView Molecular Modeling Software*, Semichem Inc., Shawnee Mission, KS, 2016.
- 46 T. Lu and F. Chen, Multiwfn: A multifunctional wavefunction analyzer, *J. Mol. Struct.*, 2012, **1006**, 84–92.
- 47 D. Brown, Geometry of O–H $\cdots$ O hydrogen bonds, *Acta Crystallogr.*, 1976, **32**, 24.
- 48 M. R. H. Blessing, Hydrogen bonding patterns in molecular systems, *Acta Crystallogr., Sect. A*, 1976, **32**, 24.
- 49 J. Tauc, Optical properties of materials, *Mater. Res. Bull.*, 1968, **3**, 37.
- 50 F. Yakuphanoglu, R. Mehrotra, A. Gupta and M. Munoz, Polymer science applications, *J. Appl. Polym. Sci.*, 2009, **114**, 794.
- 51 C. Aydin, M. S. AbdEl-Sadek, Z. Kaibo, I. S. Yahia and F. Yakuphanoglu, Advances in laser technology, *Opt. Laser Technol.*, 2013, **48**, 447.
- 52 M. Hafez, I. S. Yahia and S. Taha, Spectroscopic analysis of materials, *Spectrochim. Acta, Part A*, 2014, **127**, 521.
- 53 K. SowriBabun, A. Ramachandra Reddy, Ch. Sujatha and K. Venugopal Reddy, Ceramic materials and their properties, *Ceram. Int.*, 2013, **39**, 3055.
- 54 E. Caponetti, L. Pedone, D. Chillura Martino, V. Panto and V. Turco Liveri, Material science and engineering applications, *Mater. Sci. Eng., C*, 2003, **23**, 531.
- 55 N. Tounsi, A. Barhoumi, F. C. Akkari, M. Kanzari, H. Guermazi and S. Guermazi, Thin film properties and vacuum studies, *Vacuum*, 2015, **121**, 9.
- 56 S. R. Chalana, V. Ganesan and V. P. Mahadevan Pillai, AIP Advances in applied physics, *AIP Adv.*, 2015, **5**, 107207.
- 57 E. Toumi, N. Elleuch, S. Shova and M. Boujelbene, Structural asymmetry, physicochemical characterization and optical properties of a new luminescent zero dimensional organic-inorganic hybrid compound, *Results, Chem*, 2024, **12**, 101879.
- 58 CCDC 2384365: Experimental Crystal Structure Determination, 2025, DOI: [10.5517/ccdc.csd.cc21140t](https://doi.org/10.5517/ccdc.csd.cc21140t).

